Computer Methods and Programs in Biomedicine 251 (2024) 108203

Contents lists available at ScienceDirect

Computer Methods and Programs in Biomedicine

journal homepage: https://www.sciencedirect.com/journal/computer-methods-and-programs-in-biomedicine

An individualised 3D computational flow and particle model to predict the deposition of inhaled medicines — A case study using a nebuliser

Yulong Wang [a], Zhendong Jin [a], Yan Cui [a,*], Rongbo Dong [b], Lei Li [c], Frantisek Lizal [d], Matjaž Hriberšek [e], Jure Ravnik [e], Mingshi Yang [f], Yinshui Liu [a]

[a] School of Mechanical Science and Engineering, Huazhong University of Science and Technology, Luoyu Road 1037, 430074, Wuhan, China
[b] Department of Radiology, 95829 Hospital, Gongnongbing Road 15, 430012, Wuhan, China
[c] Department of Pediatrics, Union Hospital, Huazhong University of Science and Technology, 1277 Jie Fang Ave., 430022, Wuhan, China
[d] Faculty of Mechanical Engineering, Brno University of Technology, Technicka 2896/2, 61669, Brno, Czech Republic
[e] Faculty of Mechanical Engineering, University of Maribor, Smetanova 17, SI-2000, Maribor, Slovenia
[f] Department of Pharmacy, University of Copenhagen, Universitetsparken 2, 2100, Copenhagen, Denmark

ARTICLE INFO

Keywords:
Inhaled drug delivery
Respiratory airway
Drug deposition
Computational fluid and particle dynamics
Individualised approach

ABSTRACT

Background and objective : Drug inhalation is generally accepted as the preferred administration method for treating respiratory diseases. To achieve effective inhaled drug delivery for an individual, it is necessary to use an interdisciplinary approach that can cope with inter-individual differences. The paper aims to present an individualised pulmonary drug deposition model based on Computational Fluid and Particle Dynamics simulations within a time frame acceptable for clinical use.

Methods: We propose a model that can analyse the inhaled drug delivery efficiency based on the patient's airway geometry as well as breathing pattern, which has the potential to also serve as a tool for a sub-regional diagnosis of respiratory diseases. The particle properties and size distribution are taken for the case of drug inhalation by using nebulisers, as they are independent of the patient's breathing pattern. Finally, the inhaled drug doses that reach the deep airways of different lobe regions of the patient are studied.

Results: The numerical accuracy of the proposed model is verified by comparison with experimental results. The difference in total drug deposition fractions between the simulation and experimental results is smaller than 4.44% and 1.43% for flow rates of 60 l/min and 15 l/min, respectively. A case study involving a COVID-19 patient is conducted to illustrate the potential clinical use of the model. The study analyses the drug deposition fractions in relation to the breathing pattern, aerosol size distribution, and different lobe regions.

Conclusions: The entire process of the proposed model can be completed within 48 h, allowing an evaluation of the deposition of the inhaled drug in an individual patient's lung within a time frame acceptable for clinical use. Achieving a 48-hour time window for a single evaluation of patient-specific drug delivery enables the physician to monitor the patient's changing conditions and potentially adjust the drug administration accordingly. Furthermore, we show that the proposed methodology also offers a possibility to be extended to a detection approach for some respiratory diseases.

1. Introduction

According to a statistical report from the World Health Organisation [1], about 7.7 million people die from chronic respiratory diseases each year. In China, according to the "Healthy China Action 2019–2030" data from the National Health Commission [2], the prevalence of Chronic Obstructive Pulmonary Disease (COPD) in people aged 40 and above is 13.6%, and the total number of COPD patients is nearly 100 million. Inhaled drugs that are deposited in the alveoli can be easily absorbed due to the thin wall and large absorption surface area of the alveoli and are generally accepted as the preferred method of administration for the treatment of respiratory diseases such as asthma and COPD worldwide [3].

To achieve effective inhaled drug delivery for an individual, it is necessary to use an interdisciplinary approach that can cope with inter-individual differences. However, we note that even with such a sophisticated approach, effective therapy would also have to deal with

* Corresponding author.
E-mail addresses: yl_wang@hust.edu.cn (Y. Wang), m202270866@hust.edu.cn (Z. Jin), yan_cui@hust.edu.cn (Y. Cui), apollodong@163.com (R. Dong), lilei89@hust.edu.cn (L. Li), lizal@fme.vutbr.cz (F. Lizal), matjaz.hribersek@um.si (M. Hriberšek), jure.ravnik@um.si (J. Ravnik), mingshi.yang@sund.ku.dk (M. Yang), liuwater@hust.edu.cn (Y. Liu).

https://doi.org/10.1016/j.cmpb.2024.108203
Received 28 December 2023; Received in revised form 3 April 2024; Accepted 23 April 2024
Available online 3 May 2024

the patient's compliance to use their medication as prescribed. Moreover, the clinical conditions are more complicated than the predefined modelling conditions, and patient compliance is low [4,5]. It is a great challenge to develop individualised detection technologies.

One way to study the deposition of aerosol drugs is to use a radiolabelled nebuliser followed by gamma scintigraphy. However, if the drug deposition is measured by using radiolabelled nebulisers, patients need to take a CT scan after the test for each type of inhaled drug. Subsequently, researchers perform visualisation, segmentation, statistical analysis or modelling of PET images with specialised software to obtain the regional deposition fractions, which is more costly in terms of economy and time for patients.

Finlay et al. [6] proposed theoretical calculations to predict the pattern of lung deposition of hygroscopic aerosols in populations of normal subjects. This model also takes into account the hygroscopic growth or evaporation of aqueous nebulised drug solutions. However, the method of Finlay et al. [6] relies on computational assumptions, which reduce the dimensionality of the geometry to the 1D case, and take into account several empirical or semi-empirical models for deposition, including heat and mass transfer, together with very coarse approximations on the particle velocity and lung/air temperature and humidity. The approach has a great practical use, however, it does not distinguish between different lung geometries and associated turbulent flow fields, which have the highest impact on particle trajectories and final deposition regions.

While other established approaches adequately serve the general purpose, they fall short in distinguishing between different lung geometries, breathing rates, and associated turbulent flow fields. These factors significantly impact particle trajectories and their final deposition regions and are highly dependent on an individual's airway geometry.

In this study, we introduce an individualised model for determining pulmonary drug deposition. This model analyses the efficiency of inhaled drug delivery using Computational Fluid and Particle Dynamics (CFPD) simulations. As illustrated in Fig. 1, the physician is required to provide the patient's CT images (in 2D Dicom format) and the patient's breathing pattern. Subsequently, a 3D model of the patient's bronchial tree is reconstructed. The transient dynamic flow field within the respiratory airways is then analysed based on the patient's breathing pattern, followed by computational analysis of inhaled particle dynamics, resulting in regional drug deposition pattern, which is the basis for the final examination of the patient's drug delivery ability. Finally, a report is generated from an extensive data analysis which is returned to the physicians for further evaluation.

The proposed method offers several advantages. First, it provides an individualised detection method. A 3D geometric model of the patient's respiratory airway is constructed from 2D CT images, and the patient's breathing pattern (i.e., flow rate versus time) is recorded. Subsequently, Computational Fluid Particle Dynamics (CFPD) simulations are conducted based on these data. As a result, the analysis of drug delivery efficiency is highly individualised, as the particle trajectories depend on the interplay between the airway geometry and time-dependent flow conditions, resulting form the patient's breathing pattern. As the breathing pattern in the case of illness can be severely affected by the patient's physical conditions, the coupled airway geometry-breathing pattern analysis is of the utmost importance. Second, it allows for a sub-regional diagnosis of respiratory diseases. The proposed method can assess inhalation ability in different lung regions, such as the right upper lobe, right middle lobe, right lower lobe, left upper lobe, and left lower lobe. Furthermore, the drug delivery ability of different lobe regions can be compared with a database (e.g., patients with the same disease, sex, and age). This comparison can assist the physician in better understanding the patient's current health condition.

However, Several challenges and questions need to be addressed before applying this detection method in clinical practice. First, accurate CFPD analysis, which is complicated due to the complex structure of the bronchial tree, typically takes more than four weeks to produce results. However, doctors would prefer a processing time of 1–2 days. Therefore, it is crucial to significantly reduce the simulation time while maintaining the accuracy of the calculations for this method to be accepted in clinical practice. Second, different inhalers have varying flow resistances, which result in different breathing patterns when patients use different inhalation devices. It is infeasible to measure the breathing patterns of each patient for all inhalers. Third, the drugs emitted from pressurised metered-dose inhalers (pMDIs), soft mist inhalers (SMIs), and dry powder inhalers (DPIs) are different. The emitted dose is constant for the first two devices, while it varies depending on the patient for the last case. Moreover, the speed of the emitted particles is much higher in the case of pMDIs than in the case of SMIs and DPIs. All these factors influence drug deposition.

Therefore, this work is restricted to the presentation of the potential lying in the simulation of flow and particle transport in individual airways under realistic breathing pattern and tries to make the first step to overcome part of the impediments mentioned above. Therefore, the main aim of this work focuses on reducing the time consumption of the proposed approach to within 48 h, with acceptable accuracy in the simulation results compared with experimentally measured data. Moreover, in this study, we only investigate nebulisers since the emitted dose and drug size distribution of a nebuliser are not dependent on the patient's breathing pattern. The flow resistance of the nebuliser is much smaller compared with DPIs. Therefore, the patient's breathing pattern measured by the spirometer has a only a slight discrepancy compared with the case of nebuliser, and can be used in the CFPD analysis together with nebuliser-dependent drug dose and particle size distribution.

However, the proposed approach also has the possibility to be extended to other types of inhalers, which will be studied in the future. It is noted that the proposed approach uses the instantaneous CT data from the patient as a basis. Our approach at this point has limitations as it is based on static CT images that do not take into account the time-dependent changes in the geometry of the oropharynx, bronchoconstriction and mobile mucus.

Most computational studies use the Euler/Lagrange approach for analysing the inhaled drug deposition in vivo [7,8], which divides the calculation of CFPD into the fluid phase and the particle phase. In the fluid phase, Large Eddy Simulation (LES) or Reynolds-averaged Navier–Stokes equations (RANS), supplemented by appropriate turbulence models, are used to calculate the dynamic flow field of the respiratory airway driven by inhalation. In the particle phase, the one-way coupling is often used to track the trajectory and deposition position of drug powders/droplets in the steady or unsteady flow field of the respiratory airway. Because the size and the volume fraction of inhaled drug particles are small, i.e. particle size ranging from $0.5\ \mu m$ to $5\ \mu m$ and its volume fraction is usually below 10^{-7}, the influence of the particle on the fluid phase can be neglected.

In the Euler/Lagrange approach, the calculation speed of the particle phase is fast; most CPU time is spent calculating the flow field. However, the time step of LES has to be very small to fully resolve the generation and dissipation of large eddies in the flow field [9,10]. Therefore, To save the computational cost, RANS seems to be the best CFPD method for the proposed approach. However, a previous study [11] showed that RANS could hardly obtain the same level of Turbulent Kinetic Energy (TKE) compared to LES. As a result, the calculated particle trajectory, i.e. affected by turbulent dispersion, may have insufficient accuracy.

The paper aims to present an individualised pulmonary drug deposition model based on CFPD within a time frame acceptable for clinical use, and is organised as follows. In Section 2.1, an airway boundary identification approach is proposed to reconstruct the 3D geometric model of the respiratory airway independent of the engineer's skills. Sections 2.2 and 2.4 proposes a rapid and accurate calculation approach to the fluid phase. Section 2.5 proposes appropriate force models for

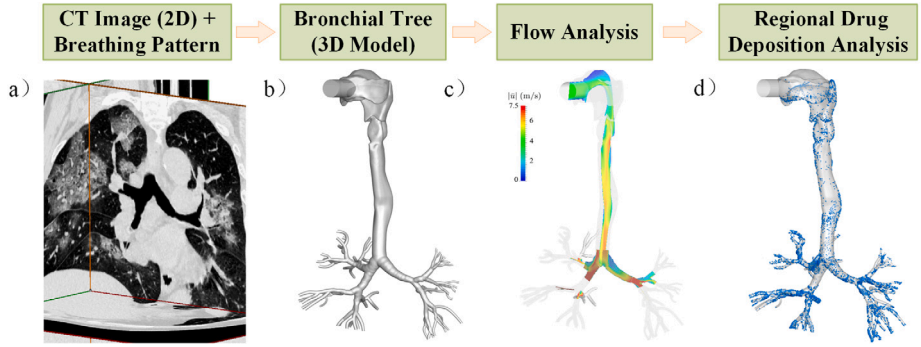

Fig. 1. Flow chart of the individualised approach to drug deposition analysis.

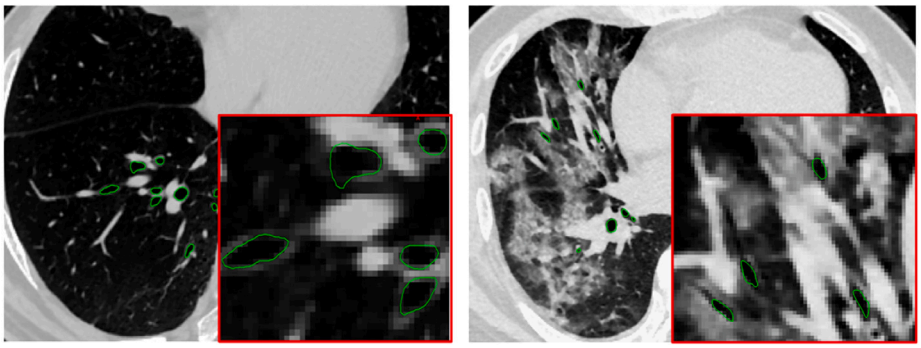

Fig. 2. Comparison of the CT image of the lung of COVID-19 patients (right) with healthy people (left) including the airway identification.

tracking inhaled drugs. In Sections 3.1 and 3.2, the simulation results are verified by comparing them with available experimental data in the literature. In order to have the same setting as the experiments, the studies in Sections 3.1 and 3.2 use a general bronchial tree geometry, fixed inhalation flow rates, and monodispersed drug particles. However, in Section 3.3, the drug inhalation ability of a COVID-19 patient is studied by applying the individualised bronchial tree geometry, dynamic breathing pattern, and drug-containing polydisperse droplets generated by a nebuliser. In Section 4, we discuss several key aspects of our study. These include the numerical discrepancies observed during experimental verification, the time analysis of our proposed approach, the numerical innovations introduced in this work, and the practical utility of our model for both physicians and patients.

2. Methods

2.1. Construction of bronchial tree 3D model

Medical imaging software such as MIMICS® (commercial software) and 3D Slicer® (open-source software) can reconstruct the 3D bronchial tree automatically. However, the accuracy of the reconstructed model by using the automatic reconstruction algorithm is usually insufficient for CFPD simulation. This software also has a manual mode: manually select the airway boundary in each 2D Dicom image. In the manual mode, it is possible to construct the 3D geometric model of the bronchial tree with good precision, but there are two technical problems to be solved:

(1) How to find several tiny airways in the 2D Dicom image? As shown in Fig. 2, the airways in Dicom images are extremely difficult to find. In the manual mode, it is necessary to go back to the adjacent image which already determined the airway, keep in mind the position of the airway in this image, and then find the airway region in the following image since the two neighbouring regions should be very close to each other. However, the manual process is very time-consuming.

(2) If the airway has only a few pixels, how to determine the boundary of the airway precisely? Once the airway is located, the boundary of the airway must be determined precisely. However, in the CT image, especially at the 7th generation of the bronchial tree, the image resolution is insufficient, and only a few pixels can be found in the airway. Therefore, it is difficult to determine the boundary of the airway precisely.

As a result, the accuracy of the identified airway boundary highly depends on the user's skills. To reach a consistent result, we propose an airway boundary identification approach, by which the accuracy of the generated airway boundary is irrelevant to user's skills. As shown in Fig. 3, the procedure of the proposed approach is as follows:

(1) Filtering of human tissues by the greyscale. Human tissues with a large difference in density from bronchial tissues in CT images, such as bones, can be removed by performing threshold filtering of the greyscale. In this study, the greyscale of DICOM images is firstly transformed into a size range between 0 and 255, and then greyscale images are filtered with threshold values. The lower threshold of the greyscale is between 45 and 60, and the upper threshold ranges from 85 to 95, depending on the CT images.
(2) Airway boundary detection. After the morphological processing, the inner and outer boundaries of the airways are detected by using the edge detection approach proposed by Canny [12]. The gradient of greyscale of two adjacent pixels increases significantly at the airway boundary. In this way, the airway boundary can be detected.
(3) Clustering of boundary points for different airways. The points at airway boundaries may belong to different airways. Therefore, it is necessary to cluster the boundary points into different groups. The clustering algorithm used in this study is the density-based spatial clustering of applications (DBSCAN) proposed by Ester et al. [13]. This algorithm relies on a density-based notion of clusters which is designed to discover clusters of arbitrary shapes.

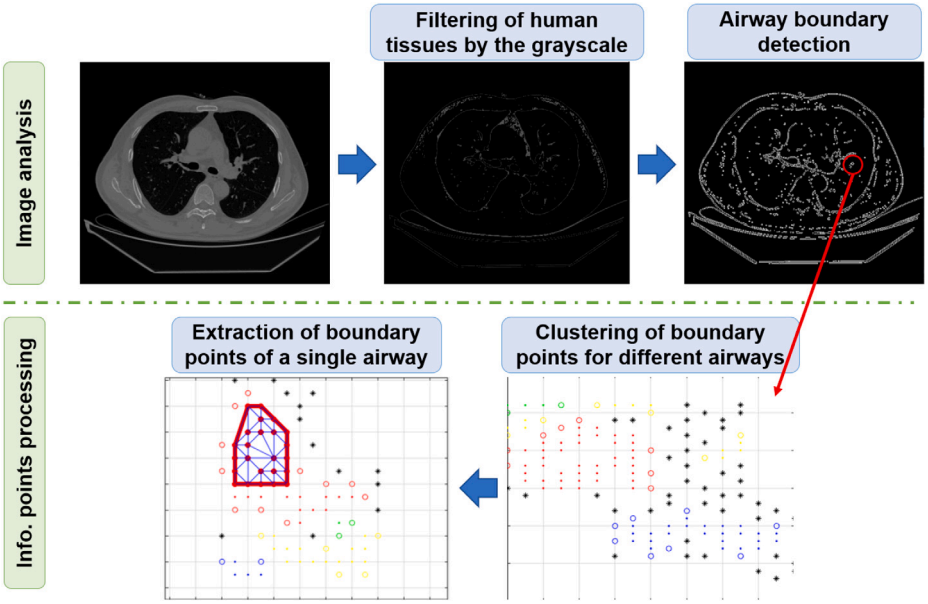

Fig. 3. Illustration of the airway boundary identification approach.

(4) Extraction of boundary points of a single airway. The boundary points of the airway on each cluster are extracted by using a Delaunay-type mesh generator [14]. In this generator, the airway is meshed by using the Delaunay triangulation mesh. Subsequently, search for the edges of all triangular mesh, and only the edges that belonged to one triangle are determined as the boundary of the airway (i.e. the red line as shown in Fig. 3). Finally, a convex hull detection is performed to optimise the airway boundary.

It should be noted that the proposed airway boundary identification approach is not an independent medical imaging software. It is only an assistant tool that assists the user in finding the airway boundary in the medical imaging software, e.g. MIMICS and 3D Slicer. The process of constructing the 3D geometry of the bronchial tree from 2D airway boundaries is still realised by using medical imaging software. Fig. 4 compares the 3D bronchial tree reconstructed by the proposed approach with the 3D bronchial tree automatically reconstructed by using MIMICS. The bronchial tree reconstructed by us can reach the 7th generation, while the one reconstructed by MIMICS only reaches the 6th generation at the lower right lobe, but the other parts of the lung only have the 4th to 5th generation of the bronchial tree. Moreover, the length of the 7th generation of the bronchial tree of the airway model using the proposed approach have a significant improvement over the model reconstructed using the automatic reconstruction algorithm of MIMICS. Fig. 5 plots part of the 3D bronchial trees reconstructed for COVID-19 and emphysema patients by using the proposed approach.

2.2. Meshing technique using fully structure mesh

In order to reduce the total number of grid elements for meshing the bronchial tree and improve the numerical accuracy of the CFPD simulation, the respiratory airway is meshed by using a fully structured mesh. In this work, ICEM is used to mesh the respiratory airway. However, many other meshing tools can also produce the same structured grid, e.g. GridPro, Ansys Mesh, and Gmsh. Fig. 6 illustrates the processes to generate a fully structured mesh of the bronchial tree. First, the respiratory airway is divided into many segments, where the structure of each segment is a bifurcation. After that, the fluid domain of each bifurcation is meshed by using a structured mesh, and the near-wall mesh is fitted to the curved surface of the airway. Subsequently, the structured meshes at the connecting surfaces of two adjacent segments are assembled. Finally, a fully structured mesh of the respiratory airway is created, as shown in Fig. 7. The total number of structured elements is approximately 8 million. The time required for the meshing lies mainly in the cutting step, i.e. cutting the respiratory airway into segments. The total time spent on meshing is about 4–6 h. The accuracy in turbulence calculation of RSM can be significantly improved by describing the near-wall region with a fine mesh. We have tested different numbers of prism layers and found that more than 15 prism layers are required to refine the near-wall region (i.e. starting at a thickness of 0.01 mm and a thickness multiplied by 1.2 in the next layer).

2.3. Turbulent models

The most accurate CFD calculation of the turbulent flow is the direct numerical simulation (DNS), which solves the unsteady motion of all turbulent flow scales. However, the difference in the turbulent time and length scales between the largest and smallest eddies of the flow in the respiratory airway can be several orders of magnitude, making the DNS calculation of the flow in the respiratory airway infeasible. The next level below DNS is LES, in which only large unsteady turbulent eddies are modelled, and small-scale dissipative turbulent eddies are assumed to be isotropic. Although the computational cost of LES is significantly reduced compared with the DNS, the computational cost for analysing the respiratory flow is still far beyond the clinical requirement.

The next lower level of sophistication is to model all the unsteady turbulent eddies with turbulence models [15]. In the case of steady and incompressible flow, the steady Navier–Stokes equation can be replaced by the RANS equation, expressed as

$$[\mathbf{u}\cdot\nabla]\,\mathbf{u} = -\frac{1}{\rho}\nabla P + \nu\nabla^2\mathbf{u} + \nabla\cdot\tau_{ij}, \tag{1}$$

where ρ, ν, P are the density, kinematic viscosity and pressure of the fluid, respectively, $\mathbf{u}$ is the fluid velocity, and τ_{ij} is the specific Reynolds stress tensor. Since τ_{ij} is symmetric, six unknown elements in the tensor are modelled in various ways by turbulence models. In the studies of Sommerfeld et al. [16] and Cui et al. [17], the TKE level of RANS in connection with the Reynolds Stress Models (RSM) has the most considerable TKE level compared with other turbulent models. RSM uses a second-order closure and is able to account for complex interactions in turbulent flow fields. In this work, RSM based on Speziale–Sarkar–Gatski (SSG) [18] is applied, in which six unknown

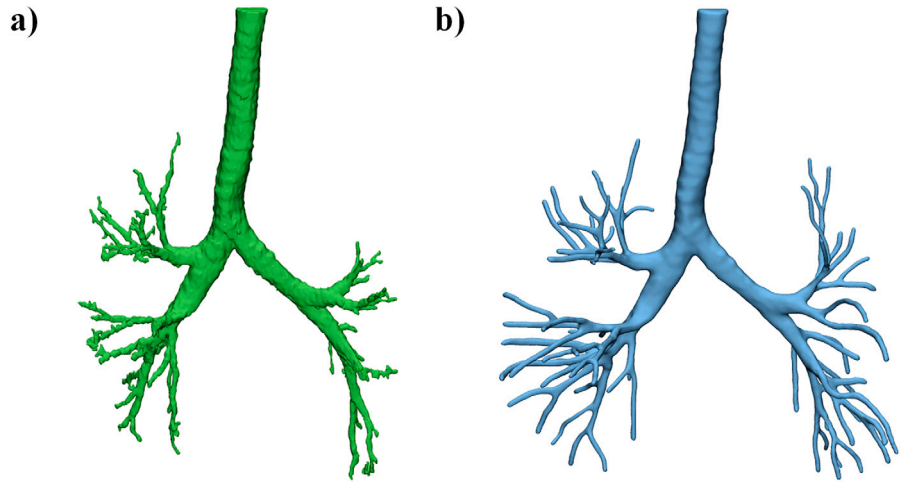

Fig. 4. Comparison of 3D bronchial tree reconstructed using different techniques: (a) automatic reconstruction algorithm of MIMICS®; (b) the proposed airway boundary identification approach.

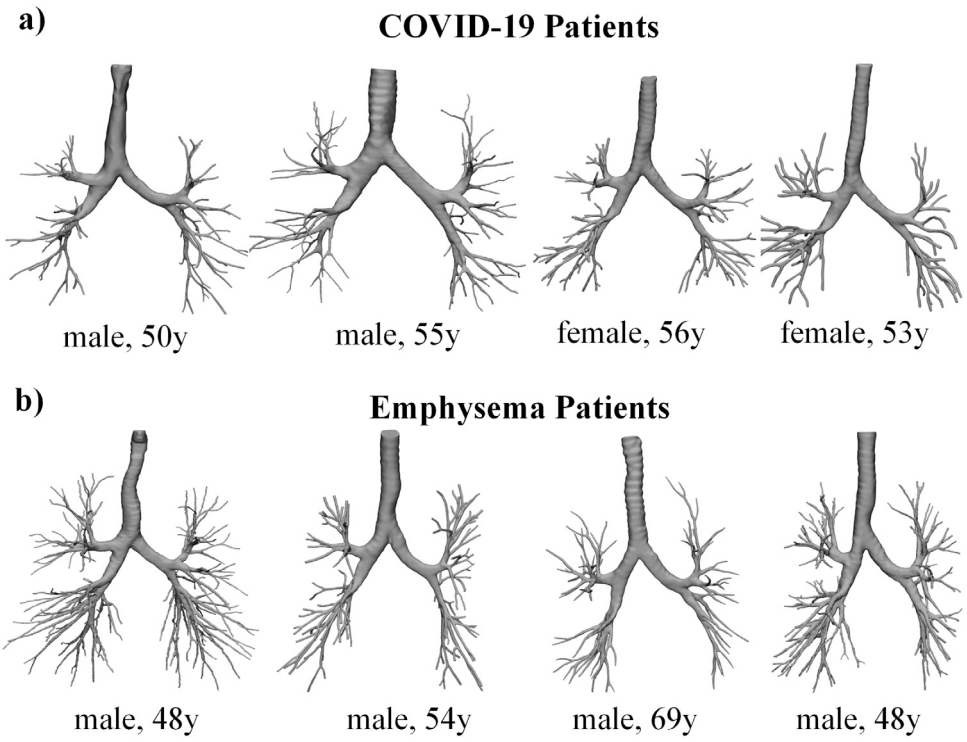

Fig. 5. Examples of the reconstructed 3D CAD models of the bronchial tree using the proposed airway boundary identification approach; (a) 3D bronchial trees of COVID-19 patients; (b) 3D bronchial trees of emphysema patients.

elements of τ_{ij} are solved by six additional transport equations. In this way, RSM-SSG has the advantage of solving the anisotropy of the complex turbulence flow of the respiratory airway [16]. We utilise a second-order upwind numerical scheme to compute conventional terms, and the Semi-Implicit Method for Pressure-Linked Equations (SIMPLE) algorithm is employed for the fluid solver. The flow phase simulation is carried out using ANSYS Fluent.

2.4. Boundary conditions

The no-slip boundary condition is applied to all walls of the fluid domain. Ambient pressure is set at the inlet, and varying mass flow rates are assigned to the outlets of different lobes of the bronchial tree. The weight factor of the flow rate at each outlet is closely tied to the cross-sectional area of the outlet. This method was proposed by Schmidt et al. [19], who constructed a highly accurate bronchial tree using a human lung from an adult male, which included 1453 bronchi up to the 17th Horsfield order. The lung volume is partitioned into regions for the lobes. Areas of reduced structural density in the high-resolution computer tomography (HRCT) data are identified as lobe boundaries using the watershed transform. By assigning each point of the lung volume to the nearest terminating leaf of the segmented bronchial tree within the same lobe, they estimated the drain volume supplied downstream by each part of the bronchial tree. From the results, they found that the drain volume is related to the cross-sectional area of their parent. Therefore, the cross-sectional area of the outlet that divides the total cross-sectional area of the outlets can be considered as the weight factor of the flow rate of this outlet.

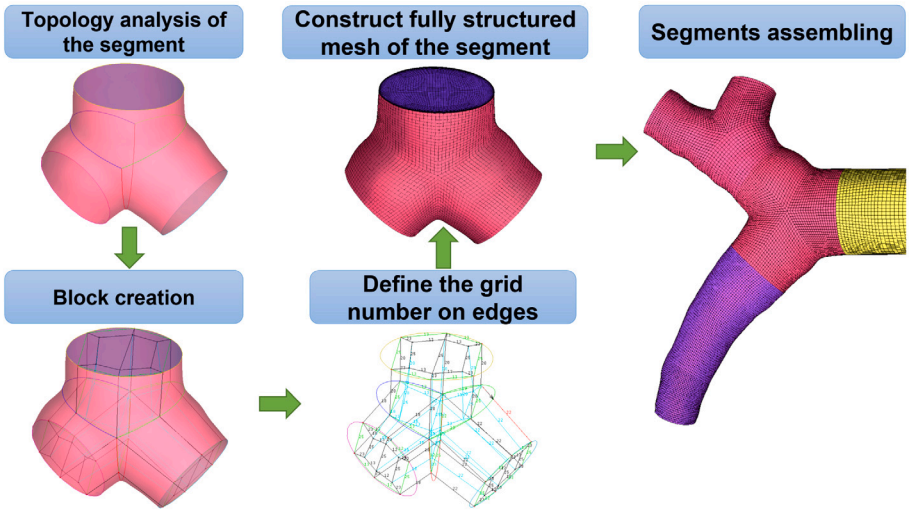

Fig. 6. Processes to generate a fully structured mesh of the bronchial tree.

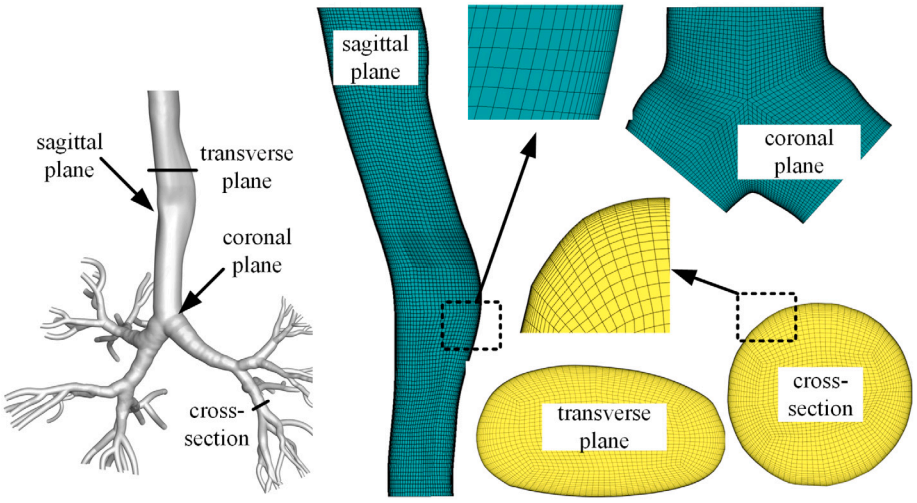

Fig. 7. Meshing the respiratory airway using a fully structured mesh and attaching more than 15 prism layers to the wall.

2.5. Forces on particles

The tracking of inhaled drug particles typically adheres to a Lagrangian approach. In this context, the particles are treated as point particles. The spatial tracking of these particles is dictated by Newton's second law of motion, which can be formulated as follows:

$$m_p \frac{d\boldsymbol{u}_p}{dt} = \sum \boldsymbol{F}_i, \tag{2}$$

where m_p and $\boldsymbol{u}_p$ are the mass of the particle and the instantaneous particle velocity, respectively. On the right-hand side of the above equation, the sum of the forces that act on the particle is represented. These forces include the drag force $\boldsymbol{F}_{\mathrm{D}}$, the gravity $\boldsymbol{F}_{\mathrm{G}}$, the shear-induced lift force $\boldsymbol{F}_{\mathrm{SL}}$, the slip-rotation lift force $\boldsymbol{F}_{\mathrm{RL}}$, the pressure gradient force $\boldsymbol{F}_{\mathrm{PG}}$ and the Brownian motion force $\boldsymbol{F}_{\mathrm{BM}}$. The buoyancy force that acts on the particle is already accounted for in the pressure gradient force.

Drag force is the most important force affecting the two-phase flow of particles. In the case of microscopic particles, i.e. $D_p < 5$ μm, Cunningham correction on the drag force must be considered [11]. The drag coefficient proposed by Schiller and Naumann [20] for particle Reynolds number $Re_p \leq 1000$ is given by:

$$C_D = \frac{24}{Re_p}\left[1 + 0.15 Re_p^{0.687}\right], \tag{3}$$

and the particle Reynolds number is defined as:

$$Re_p = \frac{D_p\,|\boldsymbol{u} - \boldsymbol{v}|}{\nu}, \tag{4}$$

where D_p, $\boldsymbol{u}$, and $\boldsymbol{v}$ are the particle size, the fluid velocity and the particle velocity, respectively. Above $Re_p = 1000$ the flow is fully turbulent, and the drag coefficient is approximately constant value: $C_D \approx 0.44$. It should be noted that the drag force of Schiller and Naumann [20] does not consider the wall effect. Goldman et al. [21] observe that the drag force acting on the particle decreases linearly with the increasing gap (i.e. the gap between the particle and the wall) in the Stokes regime. They also developed a drag force model as a function of the gap size for a stationary spherical particle in a linear shear flow, but this drag model is valid only for the Stokes flow condition. Additional modelling on the drag force acting on the particle of the near-wall region at a more extensive range of particle Reynolds numbers may be required.

The Cunningham correction factor is used to correlate the drag force for particles of comparable size to the mean free path of the fluid molecules and is given by:

$$C_D = \frac{C_D}{C_u}, \quad C_u = 1 + \frac{2\lambda}{D_p}\left[1.257 + 0.4\exp\left(-\frac{1.1 D_p}{2\lambda}\right)\right], \tag{5}$$

where $\lambda = 0.070$ μm is the mean free path of air.

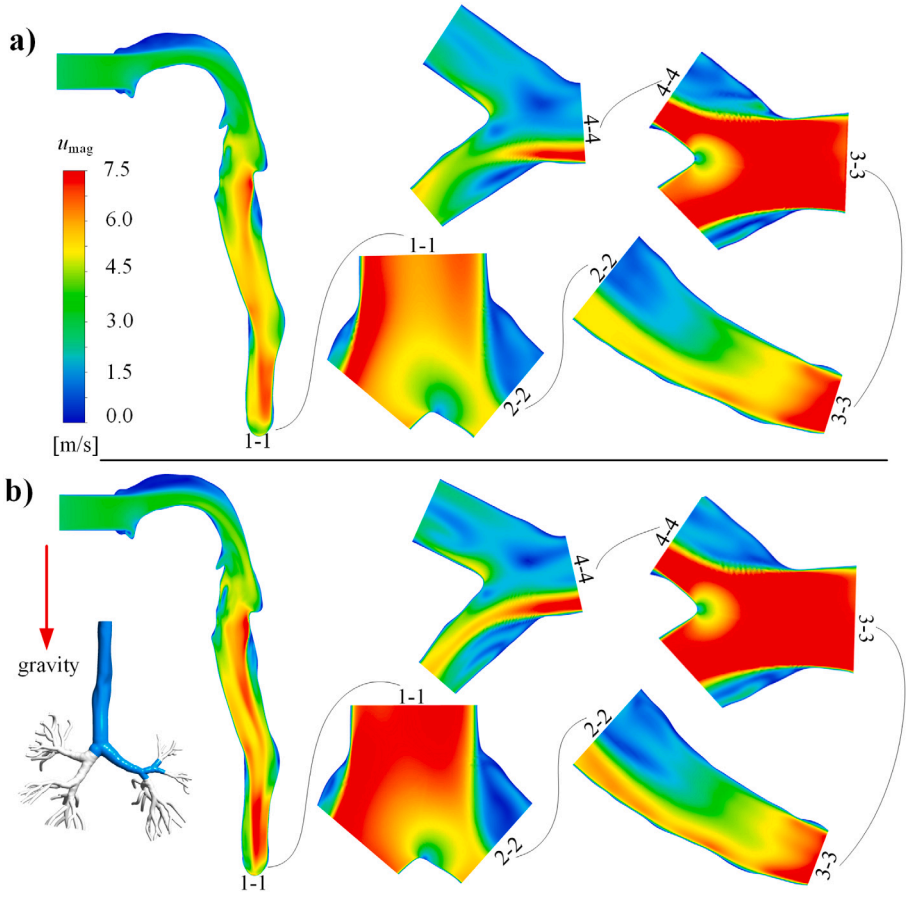

Fig. 8. Time-averaged velocity fields of the respiratory airway from the inlet to one of the outlets in the left lower lobe of the lung calculated by using LES (a) and RANS (b) (flow rate: 60 l/min, the displayed airways are highlighted blue in the bronchial tree).

Particles moving in a shear flow experience a transverse lift force. This is primarily due to the non-uniform relative velocity across the particle, which subsequently leads to a non-uniform pressure distribution. The shear-induced lift force is given by:

$$\boldsymbol{F}_{\mathrm{SL}} = \frac{\rho_f}{2}\frac{\pi}{4}D_p^2 C_{\mathrm{SL}} D_p \left[[\boldsymbol{u}-\boldsymbol{v}]\times\boldsymbol{\omega}_f\right], \tag{6}$$

where μ_f and $\boldsymbol{\omega}_f$ represent the fluid dynamic viscosity and the flow vorticity, respectively. The shear-induced lift coefficient, denoted as C_{SL}, is defined as follows:

$$C_{\mathrm{SL}} = \frac{4.1126}{Re_s^{0.5}} f(Re_p, Re_s), \tag{7}$$

where $Re_s = \rho_f D_p^2 |\boldsymbol{\omega}_f| / \mu_f$ is the shear Reynolds number. The correction function, denoted as $f(Re_p, Re_s)$, was proposed by Mei [22] and is based on calculations performed by Dandy and Dwyer [23]. This function applies to a particle Reynolds number in the range of approximately $0.1 \le Re_p \le 100$.

Particles that are not freely rotating in a flow can also experience a lift force due to their rotation, known as the Magnus force. An analytical expression for the slip-rotation lift force, applicable in the case of the Stokes flow condition, was derived by Rubinow and Keller [24]:

$$\boldsymbol{F}_{\mathrm{RL}} = \frac{\rho_f}{2}\frac{\pi}{4}D_p^3 \left[\boldsymbol{\Omega}\times[\boldsymbol{u}-\boldsymbol{v}]\right], \tag{8}$$

where $\boldsymbol{\Omega}$ is the relative rotation given by:

$$\boldsymbol{\Omega} = \frac{1}{2}\nabla\times\boldsymbol{u} - \boldsymbol{\omega}_p, \tag{9}$$

with $\boldsymbol{\omega}_p$ the particle angular velocity. The slip-rotation lift force can be extended for higher particle Reynolds numbers by introducing a rotation-induced lift coefficient, denoted as C_{RL} [25]:

$$\boldsymbol{F}_{\mathrm{RL}} = \frac{\rho_f}{2}\frac{\pi}{4}D_p^2 C_{\mathrm{RL}} |\boldsymbol{u}-\boldsymbol{v}| \frac{\boldsymbol{\Omega}\times[\boldsymbol{u}-\boldsymbol{v}]}{|\boldsymbol{\Omega}|}, \tag{10}$$

For small particle Reynolds numbers, the lift coefficient is derived according to Rubinow and Keller [24] as follows:

$$C_{\mathrm{RL}} = \frac{D_p|\boldsymbol{\Omega}|}{|\boldsymbol{u}-\boldsymbol{v}|} = \frac{Re_r}{Re_p}, \tag{11}$$

with:

$$Re_r = \frac{\rho_f D_p^2 |\boldsymbol{\Omega}|}{\mu_f}, \tag{12}$$

being the Reynolds number of particle rotation. Oesterle and Petitjean [26] proposed the following correlation, which is based on available literature data and additional experiments for particle Reynolds numbers less than 140:

$$C_{\mathrm{RL}} = 0.45 + \left[\frac{Re_r}{Re_p} - 0.45\right] exp(-0.05684 Re_r^{0.4} Re_p^{0.3}). \tag{13}$$

The local pressure gradient present in the flow results in an additional force that is directed towards the pressure gradient, which is given by:

$$\boldsymbol{F}_{\mathrm{PG}} = m_p \frac{\rho_f}{\rho_p}\left[\frac{D\boldsymbol{u}}{Dt} - \boldsymbol{g}\right]. \tag{14}$$

Sub-micro-metre particles are also subjected to Brownian motion, which is caused by random collisions with gas molecules. The equation for the Brownian motion force can be articulated as follows:

$$\boldsymbol{F}_{\mathrm{BM}} = \xi m_p \sqrt{\frac{216 k_{\mathrm{Boltz}}}{\pi \left[\rho_p/\rho_f\right]^2 C_u}} \sqrt{\frac{\nu_f T_f}{\rho_f D_p^5 \Delta t}}, \tag{15}$$

where ξ_i represents a random number within the range of 0 to 1, T_f denotes the absolute temperature of the fluid, $k_{\mathrm{Boltz}} = 1.380649 \times 10^{-23}$ J/K is the Boltzmann constant, and Δt signifies the time step used in the integration of the particle equations of motion [27]. The time step utilised in the simulation is significantly smaller than the particle's Stokes number.

In this study, a turbulent dispersion model is employed for RANS simulation to accommodate the local velocity field's turbulence-induced fluctuations. The model adopted here is a two-step Lagrangian approach, as proposed by Sommerfeld [28]. This approach supposes that the fluctuating fluid velocity encountered by a particle is a combination of two components: one that is correlated with the velocity from the previous time step, and another that is randomly derived from a Wiener process. The Lagrangian particle tracking models have been incorporated into the open-source software, ParaView®.

3. Results

3.1. Fluid phase analysis and verification

To verify the present simulation results with available experimental data in the literature [11,16,29], a general geometry model of the bronchial tree is used for numerical verification in Sections 3.1 and 3.2. For comparison, two flow rates are considered, i.e. 15 l/min and 60 l/min.

As a reference result, LES simulations equipped with the Smagorinsky subgrid-scale (SGS) model are performed. In the experiment of Sommerfeld et al. [16], the lung model is manufactured as a transparent silicone model and is immersed in a tank. The tank is filled with a water–glycerine mixture which matches the refractive index of the silicone model. The flow is generated by using a piston diaphragm pump attached to a linear actuator.

Fig. 8 shows the flow field from the inlet (i.e. mouthpiece of inhaler) to one of the outlets in the left lower lobe of the lung (i.e. the blue region of the respiratory airway in the figure). The calculated velocity field using RANS is compared to the time-averaged LES results at a flow rate of 60 l/min. Fig. 9 compares the velocity profiles at six cross-section areas along the respiratory airway. The indexes of different cross-sectional profiles are illustrated in Fig. 10. The magnitude of the fluid velocity u_{mag} is normalised by diving the bulk velocity inside the trachea u_{T} [16]. The difference in velocity profiles, as shown in Fig. 9, is further analysed in Table 1 quantitatively. The root-mean-square error (RMSE) of the normalised fluid velocity between the simulation and experimental results ranges from 0.0803 to 0.2602. It should be noted that, in the PIV measurements carried by Sommerfeld et al. [16], a water–glycerine mixture is used instead of the air to avoid optical distortion. However, in the present study, the RANS and LES simulations are performed using the air, while the inflow Reynolds number is the same as in the experiment. Therefore, the difference in viscosity could bring the discrepancy in the velocity profile near the boundary layer. By comparing the present RANS results with the LES results, the RMSE of the normalised velocity reduces significantly and ranges from 0.0374 to 0.1363.

The flow Reynolds number values (calculated by using the hydraulic diameter) at different cross-sectional profiles along the airway for RANS and LES are compared in Fig. 11, and a good agreement is found between the results. The flow Reynolds number increases in the streamwise direction at the upper respiratory airway and reaches its highest in the first respiratory tract as the cross-sectional area becomes smaller and then decreases continuously due to the increasing pressure drop.

Fig. 12 compares the calculated turbulent kinetic energy fields for RANS and LES at a flow rate of 60 l/min. The overall magnitudes of the turbulent kinetic energy of the RANS results have the same scale as the LES results. The turbulent kinetic energy k is normalised by dividing the u_{T}^2 and is then plotted in the right column of Fig. 9

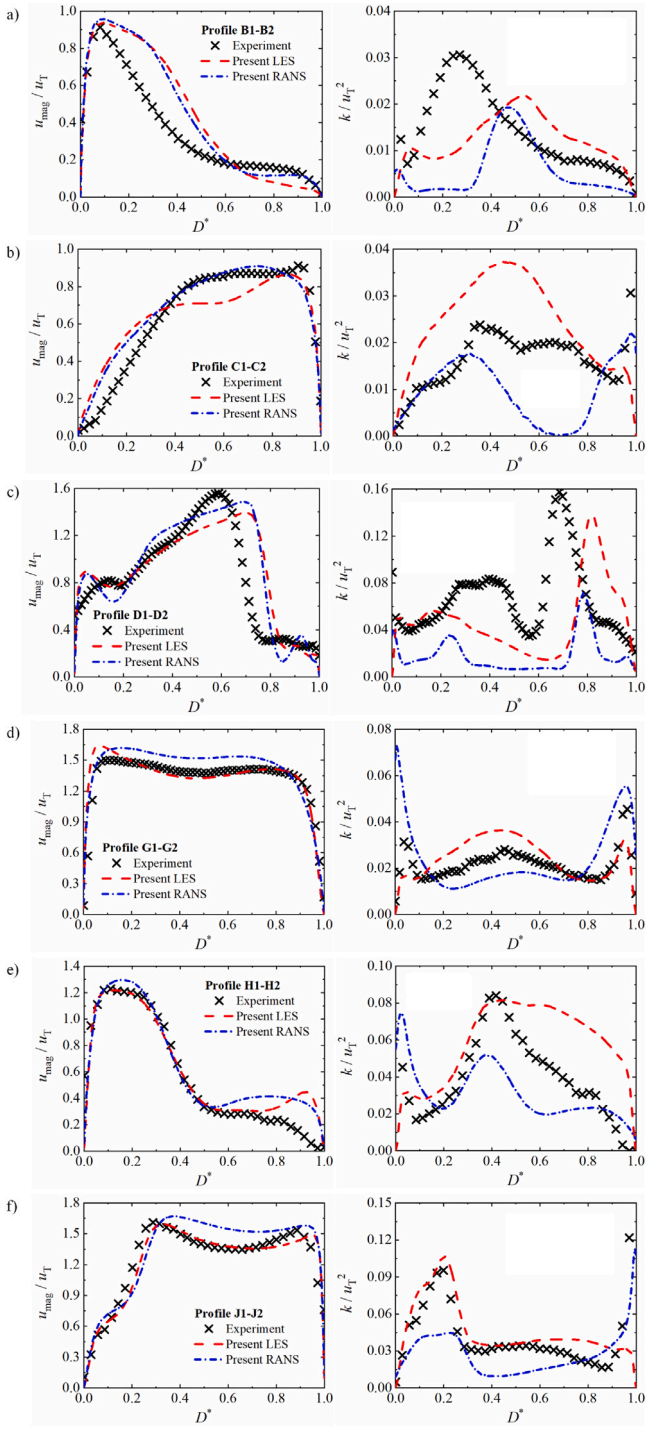

Fig. 9. Comparison of the normalised velocity (left column) and the normalised turbulent kinetic energy (left column) profiles at different cross-sectional profiles along the airway between the RANS results, the LES results and the experimental data of Sommerfeld et al. [16] (flow rate: 60 l/min, index of different cross-sectional profiles is exhibited in Fig. 10, the fluid velocity u_{mag} and the turbulent kinetic energy k are normalised in terms of the bulk velocity inside the trachea u_{T}).

for different cross-sectional profiles along the respiratory airway. The difference between the simulation and experimental results in the lower airway is smaller than in the upper airway. The RMSE of normalised turbulent kinetic energy among these profiles is presented in Table 1. The calculated RMSE of the RANS and LES simulation results compared with experimental data is between 0.0076 and 0.0588. The difference

Table 1
Root-mean-square error (RMSE) of the difference in the results as plotted in Fig. 9.

Index of the cross-sectional profiles	B1–B2	C1–C2	D1–D2	G1–G2	H1–H2	J1–J2
RMSE of LES to exp. results (u_{mag}/u_T)	0.1597	0.1152	0.2602	0.0803	0.1143	0.0826
RMSE of RANS to exp. results (u_{mag}/u_T)	0.1407	0.0815	0.2542	0.1181	0.1193	0.1577
RMSE of RANS to LES results (u_{mag}/u_T)	0.0374	0.0802	0.1101	0.1363	0.0617	0.1231
RMSE of LES to exp. results (k/u_T^2)	0.0090	0.0104	0.0541	0.0076	0.0285	0.0338
RMSE of RANS to exp. results (k/u_T^2)	0.0128	0.0103	0.0588	0.0166	0.0196	0.0223
RMSE of RANS to LES results (k/u_T^2)	0.0074	0.0185	0.0376	0.0217	0.0380	0.0354

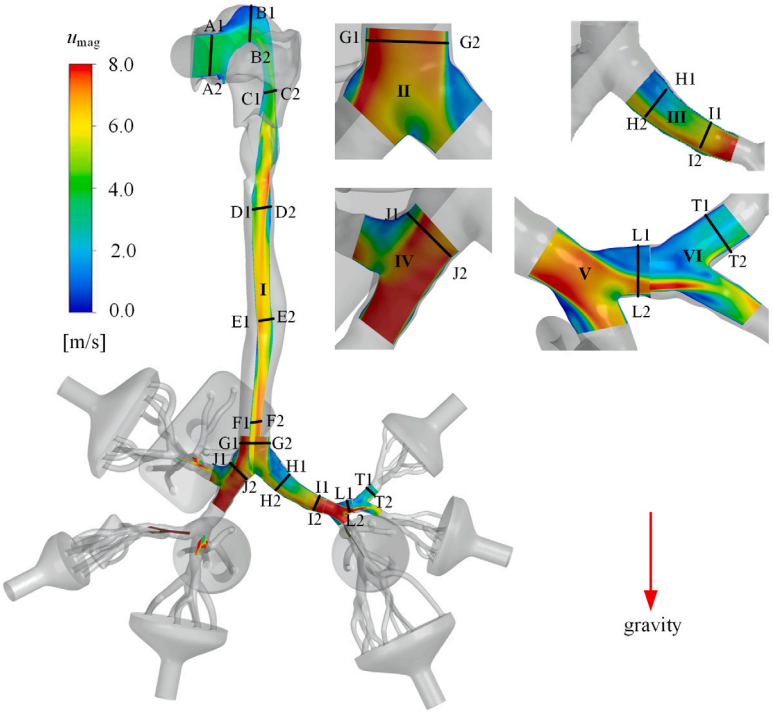

Fig. 10. Illustration of the index of different cross-sectional profiles along the respiratory airway as plotted in Figure.

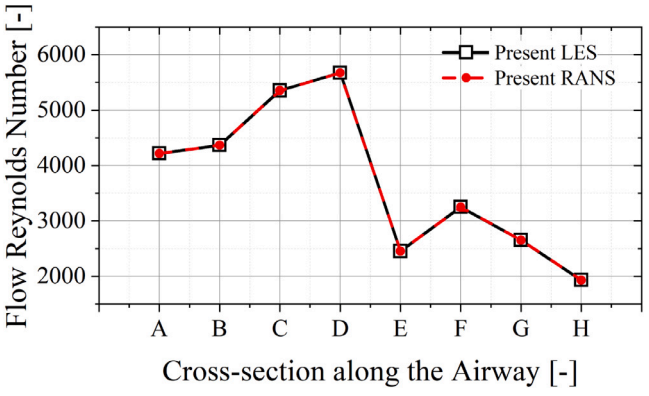

Fig. 11. Flow Reynolds number at different cross-sections along the respiratory airway (flow rate: 60 l/min).

in RMSE between the RANS and LES simulation results decreases to 0.0380. The difference in the turbulent kinetic energy between the RANS and LES simulation results improves significantly by applying the near-wall grid refinement and the RSM-SSG turbulent model.

With the help of the structured mesh, the computational cost of the RANS simulation is reduced significantly. By using a cluster equipped with 128 cores (dual-core of 2nd Gen AMD EPYC™ 7742), it takes less than 24 h for each RANS simulation.

3.2. Particle phase analysis and verification

The Lagrangian particle tracking results are verified by comparing them with the available experimental data from Lizal et al. [29]. In the experiment, a lung model was created using stereolithography with a thickness of 3 mm. This lung model is divided into 22 segments, as depicted in Fig. 13. Segments numbered 23 to 32 are ten collectors connected to the deepest level of the bronchial tree. These collectors are designed to gather particles that escape during inhalation in the experiment. Therefore, the regional deposition analysis only presents the deposition results for segments numbered 1 to 22.

The aerosol particles are generated using a condensation monodisperse aerosol generator, and radiolabelled with Fluorine 18. The particle deposition was measured by positron emission tomography (PET).

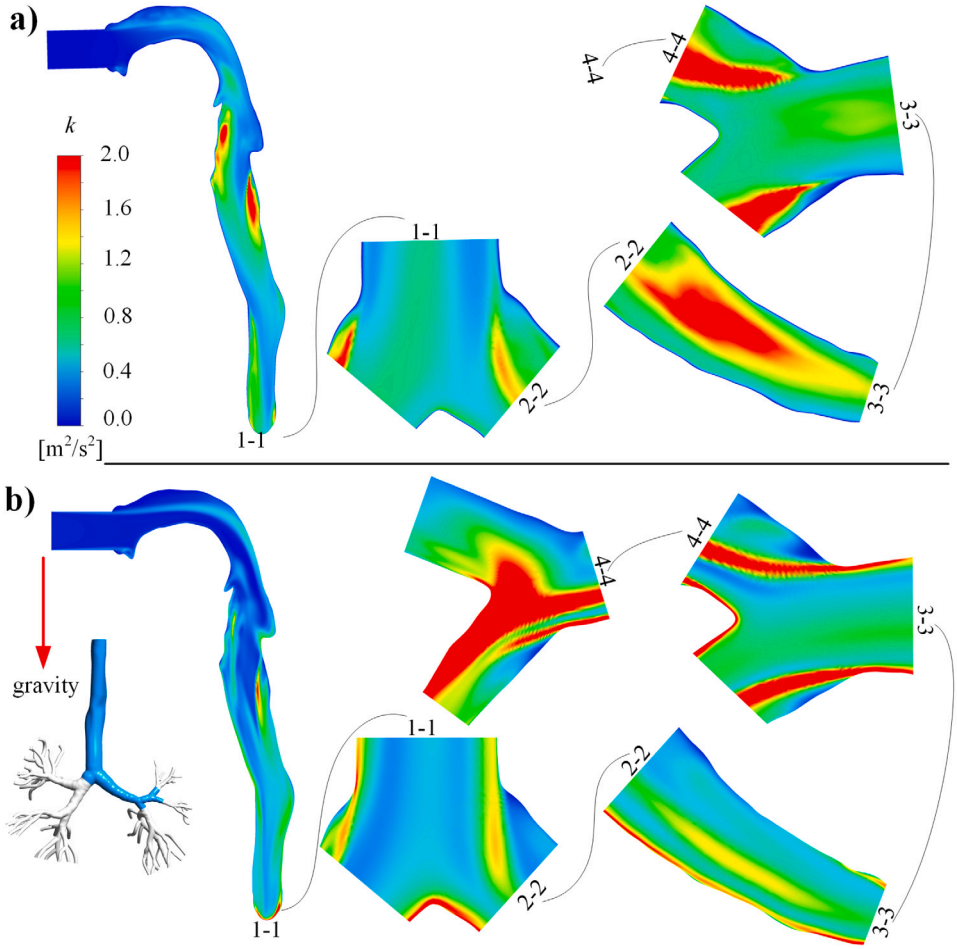

Fig. 12. Time-averaged turbulent kinetic energy fields of the respiratory airway from the inlet to one of the outlets in the left lower lobe of the lung calculated by using LES (a) and RANS (b) (flow rate: 60 l/min, the displayed airways are highlighted blue in the bronchial tree).

The monodispersed aerosol particle size is 4.3 μm, and its density is 914 kg/m^3. The particles are tracked in the fluid field calculated by using RANS and LES, respectively. In Lagrangian particle tracking, a total number of 100,000 particles are released into the airway at the inlet. These particles are tracked for 0.5 s, ensuring that the majority of the particles are deposited on the wall or escaped from the airway. In the experiment, the mucus in the respiratory airway is simulated by using silicon oil, therefore the particle is assumed to be stuck to the wall when it touches the wall.

As discussed in Section 2.4, various forces act on the particle. It is crucial to investigate which forces play important roles in inhaled particles. Subsequently, we consider the drag force associated with Cunningham correction and the gravity diminished by buoyancy as the basic force combination, denoted as F_{Basic}. For comparison, the particle trajectory is determined using F_{Basic}; other forces are computed along the trajectory but do not influence the particle. To enable a statistical study, we recorded the forces along the trajectories of 20 particles, i.e., two particles per outlet. These particles are chosen such that they can reach the Carina of the respiratory tract simultaneously at a fixed flow rate. Due to variations in flow rates, the particles exhibit different particle residence times t_{PRT}. Therefore, a dimensionless particle tracking time is introduced and defined as $t^* = t/t_{\text{PRT}}$, where t represents the dimensional particle tracking time.

Fig. 14h compares the drag coefficient with and without the Cunningham correction for different particle sizes at $Re_p = 1$. The difference in results is 3.91% for $D_p = 4.3$ μm and increases to 8.11% for $D_p = 2$ μm. It is noted that the inhaled particles exhibit a non-uniform size distribution, with a substantial fraction of particles being smaller than 2 μm. Consequently, it is necessary to include the Cunningham correction when calculating the drag coefficient.

Fig. 14a depicts the ratio of the shear-induced lift force to F_{Basic} as a function of the dimensionless particle tracking time for various flow rates. Each data point in the figure signifies the mean value of the data from 20 particles. The dimensionless particle tracking times of 0.51 and 0.77 correspond to the moments when the particles reach the Carina of the respiratory tract for flow rates of 60 l/min and 15 l/min, respectively. Furthermore, Table 2 displays the mean value and the corresponding standard deviation of all recorded data for each flow rate. This ratio tends to increase at larger flow rates, which is reasonable since the shear-induced lift force is associated with the shear rate. As illustrated in Fig. 14b, the magnitude of the velocity gradient tensor at 60 l/min is, on average, 6.5 times larger than that at 15 l/min. Notably, the shear rate at the lower respiratory tract is considerably larger than that at the upper respiratory tract, resulting in a larger ratio of $F_{\text{SL}}/F_{\text{Basic}}$ at the lower respiratory tract.

Fig. 14c presents the ratio of the slip-rotation lift force to F_{Basic} as a function of the dimensionless particle tracking time for various flow rates. This ratio tends to increase at larger flow rates, although it remains less than 0.00001. Fig. 14d further illustrates the magnitude of the relative rotation of particles along the trajectory, which is notably small and falls below 200 rad/s. Given such a minimal angular velocity, the slip-rotation lift force has a negligible influence on the motion of inhaled drug particles.

Fig. 14e depicts the ratio of the pressure gradient force to F_{Basic} along the particle trajectory for different flow rates. Generally, the values of this ratio at a flow rate of 15 l/min are larger than those at

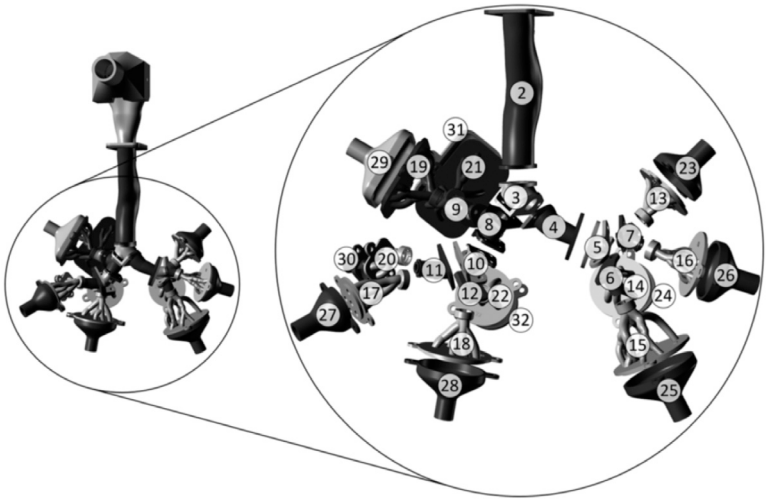

Fig. 13. The vitro experimental model: segments 1–32 of the respiratory tract [29].

Table 2
Mean values and standard derivations of the recorded data for 20 tracked particles at two different flow rates.

	Flow rate of 60 l/min	Flow rate of 15 l/min
F_{SL}/F_{Basic} [−]	1.47×10^{-2} $\pm 2.77\times10^{-2}$	4.33×10^{-3} $\pm 8.38\times10^{-3}$
F_{RL}/F_{Basic} [−]	2.39×10^{-6} $\pm 7.12\times10^{-6}$	6.02×10^{-8} $\pm 1.61\times10^{-7}$
F_{PG}/F_{Basic} [−]	1.48×10^{-4} $\pm 4.99\times10^{-4}$	3.80×10^{-3} $\pm 1.23 \times 10^{-3}$
F_{BM}/F_{Basic} [−]	1.54×10^{-4} $\pm 3.55\times10^{-4}$	3.01×10^{-3} $\pm 6.01\times10^{-3}$
$\lvert G\rvert$ $[s^{-1}]$	3657.81 ± 5163.30	563.07 ± 284.62
Ω [rad/s]	40.70 ± 154.54	1.31 ± 3.09
∇p $[N/m^2]$	656.73 ± 260.27	1707.69 ± 652.82

60 l/min. As shown in Fig. 14f, the pressure gradient at 15 l/min is approximately 2.5 times larger on average than at 60 l/min. This suggests that, compared to the drag force, the pressure gradient force could have greater importance at lower flow rates. However, considering that this ratio is less than 0.006 even at 15 l/min, the influence of the pressure gradient force on particle motion could be deemed negligible.

Fig. 14g compares the ratio of the Brownian motion force to F_{Basic} as a function of the dimensionless particle tracking time for two flow rates. At a lower flow rate, this ratio is slightly larger than that at a higher flow rate. However, the values of this ratio are less than 0.0005, suggesting that the Brownian motion force has a minor influence on particle motion within the considered particle size range.

In summary, it is important to consider both the drag force, the Cunningham correction, and the shear-induced lift force when tracking inhaled drug particles. The slip-rotation lift, the pressure gradient force, and the Brownian motion force can be reasonably neglected.

The primary deposition mechanisms for micro-sized particles are inertia and turbulent diffusion. If the particle is larger than 5 μm, inertia deposition is the dominant mechanism [11]. For smaller particles, while the inertia effect remains the dominant mechanism, the role of turbulent diffusion becomes increasingly important and cannot be neglected. As shown in Fig. 15, we compare the simulation results of regional drug deposition with and without the turbulent dispersion model. In this comparison, the turbulent model is RANS, the particle size is 4.3 μm, and the flow rate is 60 l/min. The results show that the turbulent dispersion model results in a slight increase in the total deposition fraction of particles compared to the case without the turbulent dispersion model. The difference is noticeable in segments 2, 3, 4, 5, 9, and 14 because the turbulent kinetic energy in these segments is very strong near the wall (see Fig. 12), and the particles in these segments have relatively smaller kinetic energy (i.e., due to the smaller time-averaged flow velocity as shown in Fig. 8). Therefore, the turbulent diffusion becomes stronger, and the inertia effect becomes weaker in these segments, increasing the deposition fractions.

Figs. 16a and b provide a comparative analysis of numerical and experimental deposition results of drug particles across various segment regions at flow rates of 60 l/min and 15 l/min, incorporating results from both RANS and LES simulations. In the upper respiratory tract region (segments 1 to 3), the RANS simulation results show a good correlation with the experimental results at a lower flow rate of 15 l/min. However, the LES simulation results slightly underestimate the drug deposition at the trachea (segment 2). When the flow rate is increased to 60 l/min, the LES simulation results align more closely with the experimental data than the RANS simulation results. Nevertheless, both simulation results underestimate the drug deposition fraction at the trachea. In the lower respiratory tract, both the RANS and LES simulation results align well with the experimental results across most segments. The primary deviation between the simulation and experimental results is observed in the second generation of the left bronchus (segment 4) at the flow rate of 60 l/min.

Fig. 16c illustrates the total deposition fractions derived from simulation and experimental results. The discrepancy between the total deposition fraction, calculated by RANS and LES based on the flow field, is small for both flow rates, with differences of 1.03% and 0.55% for flow rates of 60 l/min and 15 l/min, respectively. Compared to the experimentally obtained data, the total deposition fraction calculated by LES aligns well with the experimental results at both flow rates, with differences of 3.41% and 0.88% for flow rates of 60 l/min and 15 l/min, respectively. The discrepancy between the RANS simulation results and the experimental results slightly increases to 4.44% and 1.43% for flow rates of 60 l/min and 15 l/min, respectively, which is still within an acceptable range. While the LES model exhibits higher accuracy than the RANS model, it is noted that LES simulations are more computationally demanding. For clinical applications, it is advantageous to minimise the computational time of the fluid phase as much as possible. Consequently, we employ the RANS model for flow field calculations in subsequent case studies.

3.3. COVID-19 patient case study

This work is primarily focused on simulating flow and particle transport in individual airways, and as such, many aspects mentioned in the introduction are either simplified or not considered. At present, we are unable to accommodate all types of drug/device combinations and can only consider the same drug and device. If this approach can be clinically applied in the future, even using the same drug and device across a significant patient population, it could still provide valuable

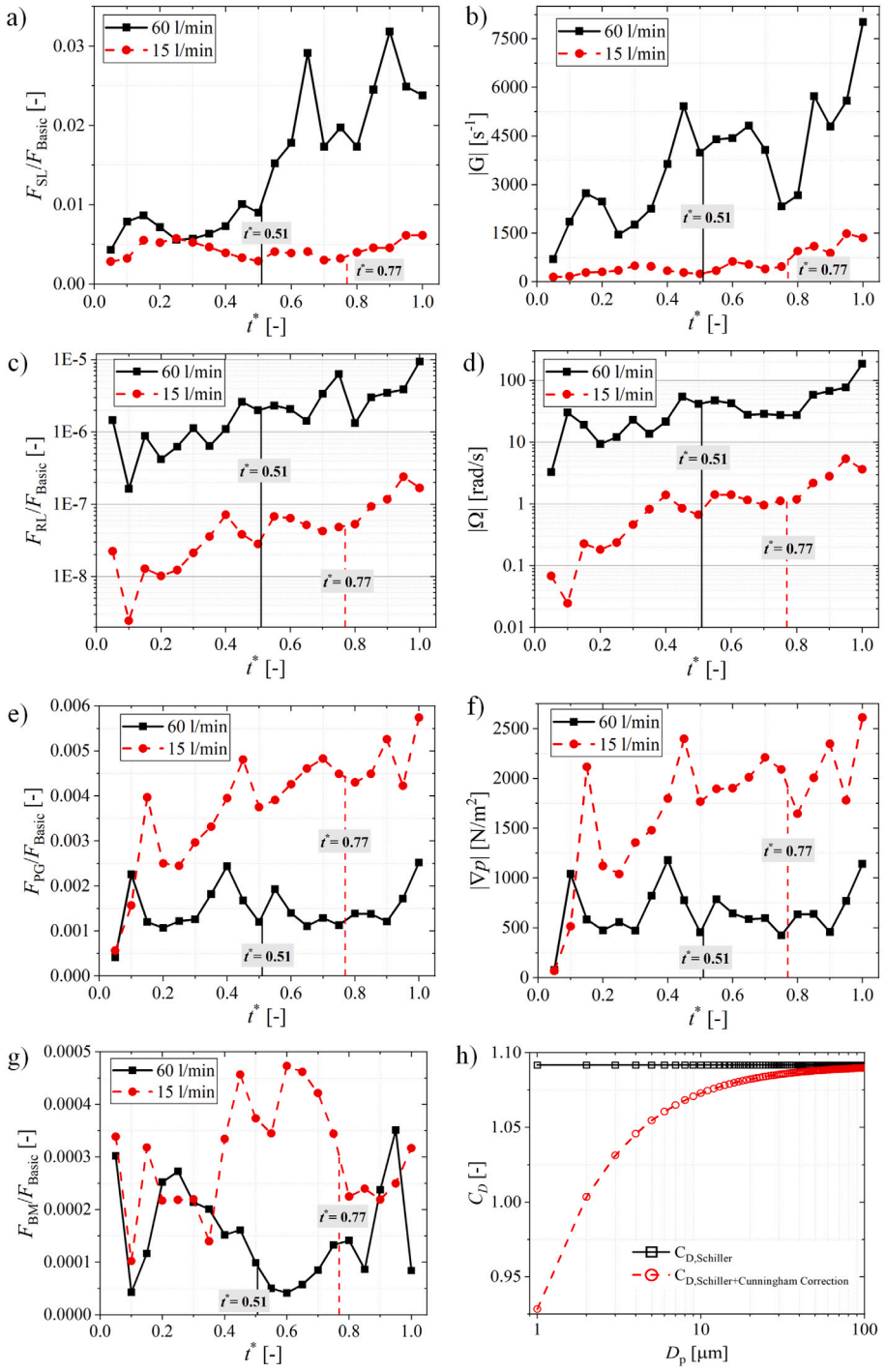

Fig. 14. This figure presents various ratios and magnitudes as functions of the dimensionless particle tracking time. Specifically, (a) shows the ratio of the shear-induced lift force to the basic force combination, (c) depicts the ratio of the slip-rotation lift force to the basic force combination, (e) illustrates the ratio of the pressure gradient force to the basic force combination, and (g) displays the ratio of the Brownian motion force to the basic force combination. The magnitudes of the velocity gradient tensor, the relative rotation, and the pressure gradient as functions of the dimensionless particle tracking time are plotted in (b), (d), and (f), respectively. Lastly, (h) compares the drag coefficient with and without the Cunningham correction for different particle sizes at Re_p= 1 (for the case of Figs. 14a to g, each data point is a mean value of 20 particles).

insights to physicians about the patient's current health condition based on database analysis. Additionally, the transport of aerosol droplets may undergo size changes due to the difference in body and room temperatures. Therefore, an isothermal condition is assumed in this work.

In this section, a case study is carried out for a COVID-19 patient (male, aged 50). As shown in Fig. 17a, the 3D bronchial tree model is reconstructed from the patient's CT scan by using the proposed airway boundary identification approach. The model contains up to the 7th generation of the bronchial tree and is divided into 10 segments. Table 3 lists the relationship between each segment and the corresponding airway regions. Because of radiation in CT scans, radiology departments in hospitals often use a slice thickness of 0.5–2 mm to scan. The thickness of two adjacent CT images is 0.625 mm for this patient. The

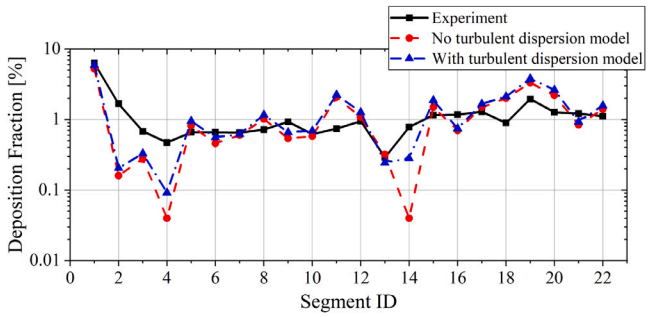

Fig. 15. Comparison of regional deposition fraction for cases with and without turbulent dispersion models. The turbulent model is RANS. The flow rate is 60 l/min. The particle size is 4.3 μm.

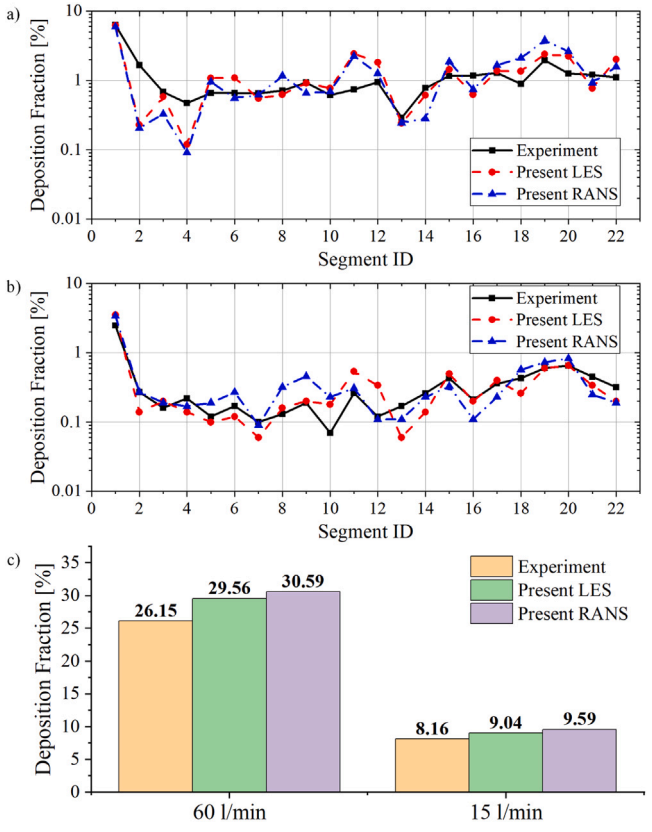

Fig. 16. Comparison of the regional deposition fraction and the total deposition fraction drug particles calculated using RANS and LES with the experimental results for two different flow rates; (a) the regional deposition fraction at a flow rate of 60 l/min; (b) the regional deposition fraction at a flow rate of 15 l/min; (c) the total deposition fraction.

7th generation of the airway model is the maximum generation that we could achieve. The total volume of the airway model is 105.9 cm^3, and its surface area is 397 cm^2. The average hydrodynamic diameter of the trachea and the 7th generation are 15.5 mm and 2 mm, respectively.

Given that the number of generations of the reconstructed bronchial tree depends on the resolution of the CT scan, it is infeasible to reconstruct the terminal bronchioles and alveoli from the CT images. However, this limitation does not pose a significant problem, as some approximations are necessary to complete the 3D computational study within a desired time slot of 48 h. As the inner diameter of the bronchi decreases with each new generation, the constricted flow area increases the probability of deposition of larger aerosol particles, while the smallest particles are more likely to reach the alveoli. From a computational perspective, this suggests that particles reaching the last generation of the 3D-modelled bronchi will most likely be deposited further down from the outlets of the computational fluid domain. In this way, the deposition pattern in the regions that are 3D modelled is not affected, and the obtained deposition results are realistic.

Table 3
The relationship between each segment and the corresponding airway regions of the geometric model of the bronchial tree of the COVID patient as plotted in Fig. 17.

Identification of segment	Airway regions
1	Oral cavity, throat and larynx
2	Trachea
3	Carina
4	Generations 2 to 4 of the left bronchus
5	Generations 2 to 4 of the right bronchus
6	Left lower lobe (LLL)
7	Left upper lobe (LUL)
8	Right lower lobe (RLL)
9	Right middle lobe (RML)
10	Right upper lobe (RUL)

The patient's breathing pattern is measured through a spirometer as shown in Fig. 17b. The peak flow rate is 60.7 l/min, and the inhalation time is about 1 s Although the simulation is performed for only one inhalation, the doses of each inhalation multiplied by the number of inhalation maneuvers can be regarded as the doses that reach the deep airway. The CFPD results can add value to the clinical use even if only the overall dose that reaches the deep airway part is predicted. A jet nebuliser with polydispersed aerosol droplets is applied, and a Rosin–Rammler distribution of aerosol size is used (see Fig. 17c) [30]. The size of aerosols ranges from 0 μm to 8 μm, and the mean diameter is 2.3 μm. The geometric standard deviation is 2.06. The density of the aerosol is 1000 kg/m^3. The aerosols start to release at $t = 0.1$ s (i.e. we assume it takes 0.1 s for aerosols to travel from the mask to the oral cavity), and 100,000 aerosols are released. At the end of the inhalation, aerosols which are not deposited or reached the outlets are not accounted for in the deposition study, as they will naturally be removed from the airway through exhalation.

Fig. 18 plots the instantaneous velocity field of the respiratory airway calculated by performing RANS simulations for different inhalation times. At $t = 0.3$ s, the flow rate is the maximum. The velocity magnitude in the oral cavity is larger than in the other region. The maximum flow velocity could reach 14 m/s. Fig. 19a plots the total deposition fraction of aerosol droplets as a function of inhalation time. The aerosols start to deposit after 0.05 s of the injection time. At the end of the inhalation, the total deposition fraction is 27.01%. It means that 72.99% of aerosol droplets can reach to the 8th generation of the respiratory airway. The deposition fraction at each segment is plotted in Fig. 19b. The deposition fraction at the oral cavity (segment 1), the LLL (segment 6), the RML (segment 9) and the RUL (segment 10) are larger than in the other regions. The deposition fraction of the LUL (segment 7) is 0.63% and is considerably lower than the other lobe regions. The deposition fraction at the trachea (segment 2) is the smallest and its value is 0.19%. This is because the main deposition mechanism is due to the inertia effect. At the trachea, there is no bifurcation and the deposition is mainly induced by turbulence diffusion.

Fig. 20a plots the deposition percentage of each size range of aerosols for different segmental regions. For each size range of aerosols, the total deposition percentage is 100%. In segment 1, aerosols in the range of 5–8 μm have the largest percentage, since these aerosols are more inertia. For the smallest size range, i.e. 0–1 μm, most of the deposition occurs at segments 1, 9 and 10, the corresponding deposition percentages are 26.47%, 29.43% and 10.78%, respectively. Fig. 20b plots the deposition percentage in each segment for different aerosol size ranges. In each segment, the total deposition percentage is 100% for all aerosol size ranges. Analysing the cumulative mass fraction figure for particle size under the Rosin–Rammler distribution reveals some

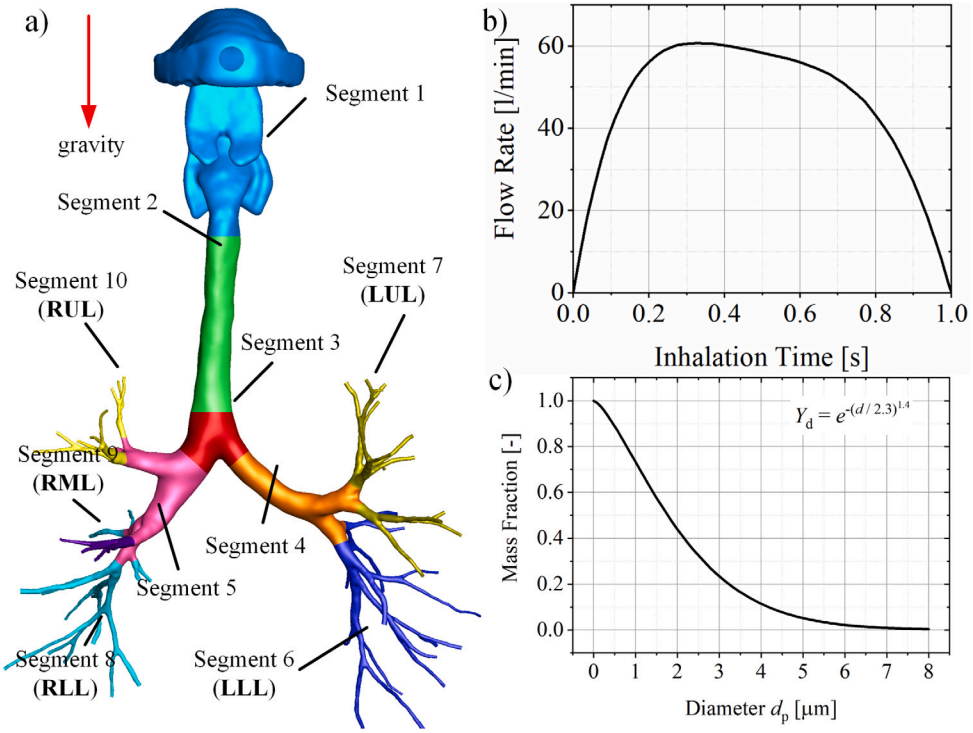

Fig. 17. The reconstructed geometric model of the bronchial tree of a COVID-19 patient (a) (male, 50 years old), the breathing pattern of the patient (b), and the size distribution of the aerosol droplet generated by a jet nebuliser (c).

key observations. Specifically, when the average particle size is 2.3 μm, there are very few particles with a diameter larger than 5 μm, and the majority of particles fall within the 1–4 μm range. Consequently, when checking the deposited particles in each section of the respiratory tract, it becomes evident that the largest proportion consists of particles in the 0–3 μm range. Furthermore, particles with diameters between 5–8 μm are primarily distributed in the upper respiratory tract, while the 0–4 μm particles are predominantly found in the small bronchi within the pulmonary lobes. This distribution pattern underscores the significant role that particle size plays in their deposition within distinct regions of the respiratory system. In general, the deposition percentage of all segments increases with increasing aerosol size. Therefore, for the design of the nebuliser, it is important to reduce the generated aerosol size to as small as possible.

The inhalation ability of different lobe regions of the lung is plotted in Fig. 21. The total drug inhalation percentage is 72.99%. It should be noted that the inhalation ability for the lobes is the fractions deposited in the generation larger than the 7th. However, some targeted receptors (e.g. beta receptors) and inhalation corticosteroids are predominantly in the deep airways. The deep airway has not been analysed because:

(1) Due to the limitations of CT resolution (i.e. slice thickness between 0.5–2 mm), 7th generation is the smallest airway to be reconstructed.
(2) The 1st to 7th generations of the airways are wrapped by cartilage, and their shape only changes slightly during inhalation. However, the geometry of the small airway changes with inhalation/exhalation. The corresponding computational cost will increase significantly by using the immersed boundary condition to solve the dynamic boundary, making the proposed approach not applicable to clinical practice.

The inhalation ability of the RML of the patient is the largest, whereas the LUL has the smallest drug inhalation percentage. The overall inhalation ability of the right lobe is larger than the left lobe (i.e. 51.69% compared with 21.31%). The physician can understand the drug inhalation ability for different lobe regions of the patient by comparing his data with a sufficiently large database.

4. Discussion

4.1. Analysis of discrepancies between simulation and experimental results

Fig. 9 compares the simulation and experimental results for the fluid phase. The discrepancy could be attributed to the different fluids used in each case. Air was used in the simulation, while a mixture of water and glycerin was used in the experiment. In the context of fully developed turbulent pipe flow, the difference between the two cases at the turbulent layer is minimal for the same Reynolds number, given that the shear rate is nearly zero. However, differences in turbulent properties become evident in the viscous sublayer, the buffer layer and the overlap layer. For instance, at the viscous layer, the wall shear stress (which is proportional to the fluid density and the square of the fluid kinematic viscosity) in the water–glycerin case is 237 times larger than in the air case. It is noted that this calculation is only applicable for fully developed turbulent pipe flow. The flow within the respiratory airway is more complex, hence the difference in fluids could lead to variations in velocity and turbulent profiles. Additionally, the RANS and LES turbulent models could introduce further errors as they are based on certain assumptions and the small eddies are not resolved. If the fluid phase is solved using DNS, the fluid field will be the most accurate. However, due to its significant computational costs, DNS may not be suitable for this application at the moment.

Fig. 16 presents a comparison between the simulation and experimental results for the particle phase. The total fraction is the sum of all drugs deposited in all segments divided by the number of emitted drugs at the end of inhalation. Indeed, the numerical error in calculating the fluid phase will impact the accuracy of the particle tracking results. Additionally, the numerical error in the particle phase could also arise from the wall effect. When a particle moves towards the wall, the wall-induced lift force pushes the particle away from the wall, resulting in a decrease in the deposition fraction. This could explain why our total deposition fraction is slightly higher than the experimental results. At a lower flow rate, the flow velocity is much smaller and the wall-induced lift force also decreases. Therefore, the numerical results align better

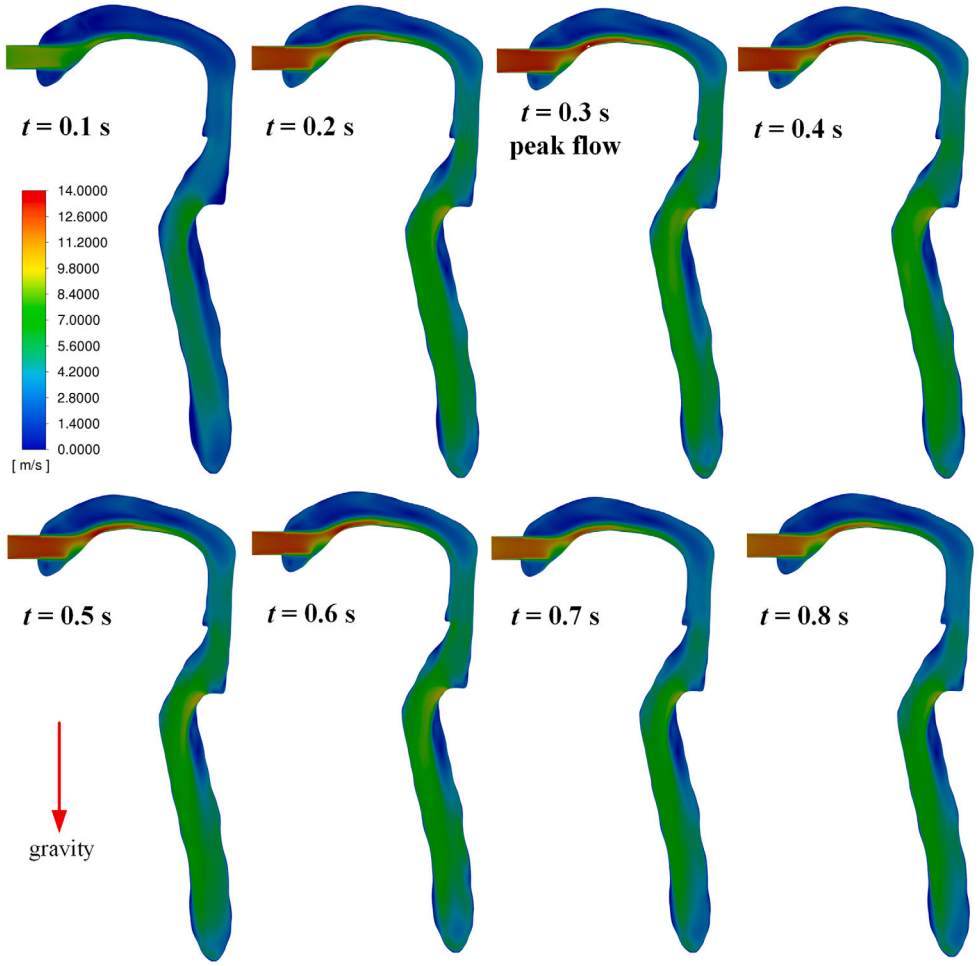

Fig. 18. Instantaneous velocity fields of segments 1 to 3 of the respiratory airway for different inhalation times; a realistic breathing pattern is applied as shown in Fig. 17b.

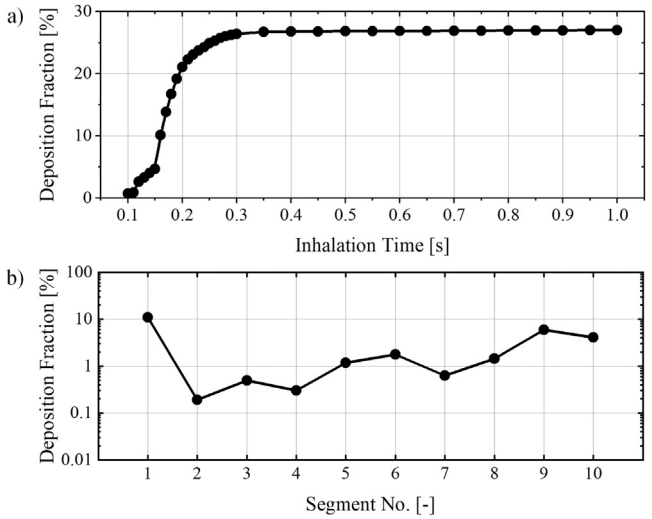

Fig. 19. Total deposition fraction of aerosols as a function of inhalation time (a) and regional deposition fraction of aerosols for different segments of the respiratory airway (b) as shown in Fig. 17a.

with the experimental results at a lower flow rate. However, we have tested the wall-induced lift force model in the literature and found it is unsuitable for the current case, leading to unreasonable results. Developing a suitable wall-induced lift force model for inhaled drug particles will be our future work.

4.2. Time analysis of the approach

The entire technical process, depicted in Fig. 22, can be completed within 48 h without compromising the accuracy of CFPD calculations. The process includes the airway boundary identification approach to reconstruct the 3D geometric model of the respiratory airways that is independent of the skills of the user (6–12 h), the use of structured grids to discretise the 3D bronchial tree (4–6 h), the computational RANS based simulation of the fluid flow in the respiratory airways (less than 24 h), and the analysis of the regional drug delivery ability (1–2 h including data post-processing). A significant effort is devoted to the most important mechanism, fluid flow, and particle-related aerodynamic forces, with the aim of improving the 3D and time-dependent computational solution of the respiratory airways as accurately and realistically as possible. The proposed approach is a comprehensive and direct 3D approach, as well as time-resolved in terms of particle dynamics, and is therefore ready to be used on a personalised level. In total, the entire process takes 35–44 h.

4.3. The numerical innovation

In the fluid phase, this study's innovation lies in reducing the simulation time from 2–4 weeks to less than 24 h to meet clinical needs. In the study of Koullapis et al. [11], each fluid phase simulation took 25 days, with a relative error of 22.22% between simulation and

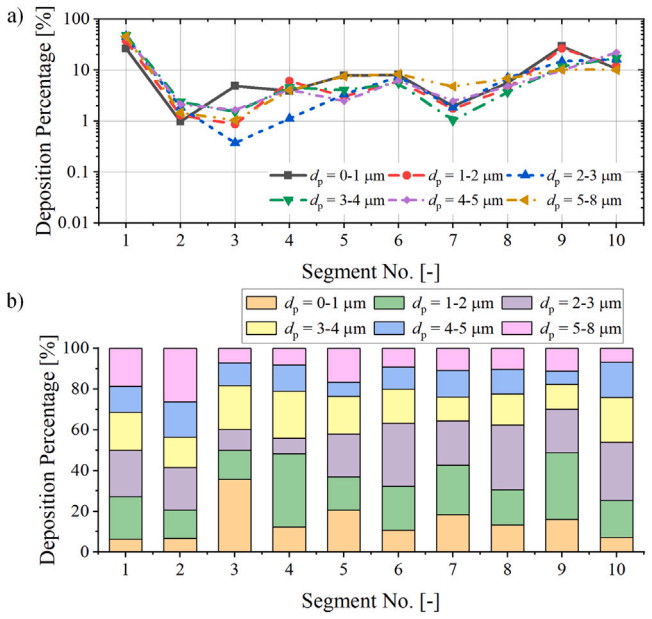

Fig. 20. Deposition percentage of each aerosol size range for different segments (a) and deposition percentage in each segment for different aerosol size ranges (b).

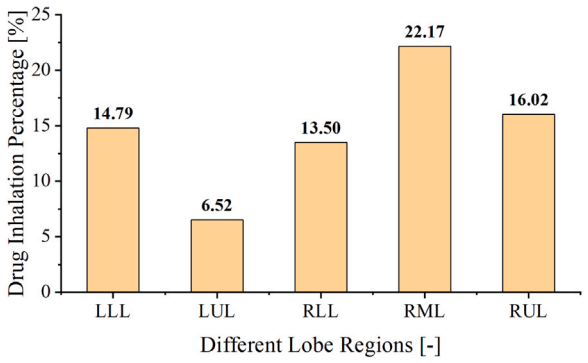

Fig. 21. Distribution of inhaled drug particles for different regions of the lung.

experimental results for a flow rate of 60 l/min. However, by using our approach, the simulation time for the fluid phase is reduced to 24 h, and the relative error between simulation and experimental results is reduced to 13.04% and 16.98% for LES and RANS, respectively, at the same flow rate. This approach reduces the simulation time and improves the numerical accuracy of the fluid phase, making it possible for clinical use.

In the particle phase, this study's innovation is developing an efficient and accurate in-house Lagrangian particle tracking code based on the open-source software Paraview®. The main advantage of this code is its high compatibility, allowing it to import fluid phase data calculated by any CFD software. Most CFD software, such as Ansys Fluent®, requires simultaneous calculation of the fluid and particle phases. Therefore, if one changes the particle properties, the software needs to recalculate the fluid phase, increasing the simulation time. However, in clinical applications, physicians may need to test different combinations of drugs and inhalers to find the optimal one for the patient. Some open-source software, such as OpenFoam®, allows separate calculations of the particle phase. However, they can only use the fluid phase calculated by this CFD software and are incompatible with other CFD software. In practice, many CFD engineers are only familiar with commercial CFD software and may struggle with open-source CFD software due to the lack of a graphical user interface (GUI). However, by using our in-house Lagrangian particle tracking code, CFD engineers can export the data of any commercial CFD software to the standard VTK format and import it into our code. Since our code also has a GUI, it would be much easier for CFD engineers to calculate the particle phase efficiently.

4.4. The practical utility of the proposed model for physicians and patients

The proposed model evaluates drug delivery efficiency based on the patient's bronchial tree geometry and breathing pattern. Changes in these factors lead to differences in the fluid field, inhalation flow rate, and flow rate distribution in different lung regions. As the drug particle trajectories depend on the interplay between the airway geometry and time-dependent flow conditions, resulting from the patient's breathing pattern, the computational analysis of drug delivery efficiency is highly individualised. As the breathing pattern in the case of illness can be severely affected by the patient's physical conditions, the coupled airway geometry-breathing pattern analysis is of the utmost importance for obtaining realistic results.

When a physician first meets a patient, the model can calculate the regional drug deposition fraction in different lung regions based on the current patient's physical conditions. Since the particle phase calculation is quick and independent of the fluid phase simulation, the physician can test various drug and inhaler combinations to find the best one for the patient. By comparing this patient's regional drug inhalation efficiency with a larger database (e.g., patients of the same disease, gender, and age), the physician can identify less functional lung regions and improve the patient's treatment.

During follow-up visits, the physician can compare new numerical simulation data with previous data to assess the effectiveness of the treatment because the patient's bronchial tree geometry and breathing pattern may change during treatment, which can easily be addressed by the developed CFPD simulation. The physician can also test different drug and inhaler combinations again to find the best one for the new treatment stage.

From the patient's perspective, this 3D approach allows them to visualise the dynamic flow field and drug deposition results in their lungs through animations. Compared to other complex medical data (e.g., test reports or CT images), this method of data presentation could enhance the trust between patients and physicians.

5. Conclusion

To achieve effective inhaled drug delivery for an individual, an individualised 3D computational flow and particle model to predict the deposition of inhaled medicines is proposed. The proposed model allows for the analysis of inhaled drug delivery efficiency and has potential applications in the sub-regional detection of respiratory diseases. The numerical accuracy of the proposed model is verified by comparison with experimental results. A case study involving a COVID-19 patient is conducted to illustrate the potential clinical use of the model. The entire process of applying the proposed model can be completed within 48 h, allowing an evaluation of the deposition of the inhaled drug in an individual patient's lung within a time frame acceptable for clinical use. As the breathing pattern in the case of illness can be severely affected by the patient's physical conditions, the coupled airways geometry-breathing pattern analysis (CFPD) offers an excellent basis for the physician to adapt the drug administration to the new physical conditions of the patient, which can significantly improve the speed of the patient's recovery. Furthermore, we show that the proposed methodology also offers a possibility to be extended to a detection approach for some respiratory diseases.

Based on the developed methodology on how to design and perform a (relatively) fast computational study of flow and particle motion in a 3D reconstructed individual lung, it is possible to also include additional phenomena into the computational model, for example, flow

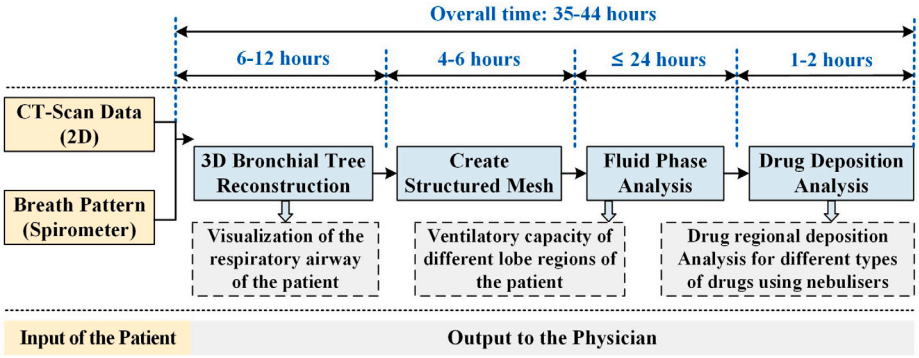

Fig. 22. Flow chart of the methodology and the time required for each technical process of the proposed approach.

based on the use of heat and mass transfer models of evaporation or hygroscopic growth. Furthermore, a higher-precision computation services could be provided using LES based fluid flow simulation for patients who require surgery (e.g. lung cancer), since the computational time requirements in case of these patients are not limited to 48 h.

At the current stage, our model is limited to nebulisers, but it holds the potential to be adapted for other types of inhalers. It is noted that physicians follow certain protocols when selecting a device–drug pair for a patient. As such, the combination of inhalers and drugs could only be among products of the same type. Furthermore, our proposed approach uses instantaneous CT data from the patient as a foundation and does not account for time-dependent changes in the geometry of the oropharynx, bronchoconstriction, and mobile mucus.

In the long run, the additional validation of the developed methodology would certainly need to be performed based on additional data from clinical studies, approved by an Ethical Committee, to test the applicability and safety of the proposed methodology. As the methodology builds on clinical techniques, which have already been proven clinically safe, we see no obstacles in its final clinical implementation.

Funding

The authors would like to express their gratitude for the financial support provided by the joint Chinese-Slovenian bilateral research project BI-CN/20-22-002, which is funded by the Slovenian Research Agency and the Ministry of Science and Technology of China. Additionally, they acknowledge the funding from the Czech Science Foundation, project GA 20-27653S.

CRediT authorship contribution statement

Yulong Wang: Writing – original draft, Visualization, Methodology, Investigation, Formal analysis, Data curation, Conceptualization. **Zhendong Jin:** Software, Methodology, Formal analysis, Data curation. **Yan Cui:** Writing – review & editing, Writing – original draft, Supervision, Resources, Project administration, Funding acquisition, Conceptualization. **Rongbo Dong:** Validation, Resources. **Lei Li:** Validation, Resources. **Frantisek Lizal:** Resources. **Matjaž Hriberšek:** Writing – review & editing, Supervision. **Jure Ravnik:** Writing – review & editing, Supervision. **Mingshi Yang:** Writing – review & editing. **Yinshui Liu:** Writing – review & editing.

Declaration of competing interest

The authors declare that they have no known competing financial interests or personal relationships that could have appeared to influence the work reported in this paper.

Data availability

The data that support the findings of this study are available from the corresponding author upon reasonable request.

References

[1] World Health Organization, World health statistics 2019: monitoring health for the SDGs, sustainable development goals, 2019.
[2] National Health Commission of the People's Republic of China 2019. Health China Action (2019-2030).
[3] W. Cheng, J. Duan, A. Zhou, Y. Zhao, R. Yi, Y. Liu, D. Deng, X. Li, Y. Zeng, Y. Peng, Q. Song, L. Lin, M. Yang, P. Chen, Real-world effectiveness of inhalation therapy among patients with symptomatic COPD in china: A multicenter prospective study, Front. Pharmacol. 12 (2021) http://dx.doi.org/10.3389/fphar.2021.753653.
[4] M. Sabz, R. Kamali, S. Ahmadizade, Numerical simulation of magnetic drug targeting to a tumor in the simplified model of the human lung, Comput. Methods Programs Biomed. 172 (2019) 11–24, http://dx.doi.org/10.1016/j.cmpb.2019.02.001, URL: https://www.sciencedirect.com/science/article/pii/S0169260718316043.
[5] Y. Guo, H. Bera, C. Shi, L. Zhang, D. Cun, M. Yang, Pharmaceutical strategies to extend pulmonary exposure of inhaled medicines, Acta Pharmaceutica Sinica. B (2021) http://dx.doi.org/10.1016/j.apsb.2021.05.015.
[6] W.H. Finlay, K.W. Stapleton, H.K. Chan, P. Zuberbuhler, I. Gonda, Regional deposition of inhaled hygroscopic aerosols: in vivo SPECT compared with mathematical modeling, J. Appl. Physiol. 81 (1996) 374–383, http://dx.doi.org/10.1152/jappl.1996.81.1.374.
[7] H. Mortazavy beni, K. Hassani, S. Khorramymehr, In silico investigation of sneezing in a full real human upper airway using computational fluid dynamics method, Comput. Methods Programs Biomed. 177 (2019) 203–209, http://dx.doi.org/10.1016/j.cmpb.2019.05.031.
[8] M. Sommerfeld, Numerical methods for dispersed multiphase flows, Part. Flows (2017) 327–396, http://dx.doi.org/10.1007/978-3-319-60282-0_6.
[9] S. Tanabe, S.R. Gopireddy, H. Minami, S. Ando, N.A. Urbanetz, R. Scherließ, Influence of particle size and blender size on blending performance of bi-component granular mixing: A DEM and experimental study, Eur. J. Pharmaceut. Sci. 134 (2019) 205–218, http://dx.doi.org/10.1016/j.ejps.2019.04.024.
[10] I. Rodriguez, O. Lehmkuhl, M. Soria, On the effects of the free-stream turbulence on the heat transfer from a sphere, Int. J. Heat Mass Transfer 164 (2021) 120579, http://dx.doi.org/10.1016/j.ijheatmasstransfer.2020.120579.
[11] P. Koullapis, S. Kassinos, J. Muela, C. Perez-Segarra, J. Rigola, O. Lehmkuhl, Y. Cui, M. Sommerfeld, J. Elcner, M. Jicha, I. Saveljic, N. Filipovic, F. Lizal, L. Nicolaou, Regional aerosol deposition in the human airways: The SimInhale benchmark case and a critical assessment of in silico methods, Eur. J. Pharmaceut. Sci. (2017) http://dx.doi.org/10.1016/j.ejps.2017.09.003.
[12] J. Canny, A computational approach to edge detection, IEEE Transactions on Pattern Analysis and Machine Intelligence PAMI-8 (1986) 679–698, http://dx.doi.org/10.1109/tpami.1986.4767851.
[13] M. Ester, H.P. Kriegel, J. Sander, X. Xu, A density-based algorithm for discovering clusters in large spatial databases with noise, in: Proceedings of the Second International Conference on Knowledge Discovery and Data Mining, 1996, pp. 226–231.
[14] H. Borouchaki, P.L. George, Aspects of 2-d delaunay mesh generation, Internat. J. Numer. Methods Engrg. 40 (1997) 1957–1975, http://dx.doi.org/10.1002/(sici)1097-0207(19970615)40:11<1957::aid-nme147>3.0.co;2-6.
[15] J.C. Yunus Cengel, Fluid Mechanics: Fundamentals and Applications, Mcgraw Hill Book Co, 2017, URL: https://www.ebook.de/de/product/29153549/yunus_cengel_john_cimbala_fluid_mechanics_fundamentals_and_applications.html.

[16] M. Sommerfeld, O. Sgrott, M. Taborda, P. Koullapis, K. Bauer, S. Kassinos, Analysis of flow field and turbulence predictions in a lung model applying RANS and implications for particle deposition, Eur. J. Pharmaceut. Sci. 166 (2021) 105959, http://dx.doi.org/10.1016/j.ejps.2021.105959.

[17] Y. Cui, Y. Wang, R. Dong, L. Li, H. Li, S. Ma, Y. Liu, Analysis of turbulent simulation method of realistic human respiratory airway, Chinese Hydraulics Pneumat. 46 (2022) 62–73, http://dx.doi.org/10.11832/j.issn.1000-4858.2022.05.007.

[18] C.G. Speziale, S. Sarkar, T.B. Gatski, Modelling the pressure–strain correlation of turbulence: an invariant dynamical systems approach, J. Fluid Mech. 227 (1991) 245–272, http://dx.doi.org/10.1017/s0022112091000101.

[19] A. Schmidt, S. Zidowitz, A. Kriete, T. Denhard, S. Krass, H.-O. Peitgen, A digital reference model of the human bronchial tree, Comput. Med. Imaging Graph. 28 (2004) 203–211, http://dx.doi.org/10.1016/j.compmedimag.2004.01.001, URL: https://www.sciencedirect.com/science/article/pii/S0895611104000187.

[20] L. Schiller, A. Naumann, Uber die grundegenden berch-nungen bei der schwerkraftaufbereitung, Z.Ver. Deut. Ing. 77 (1933) 318–320.

[21] A. Goldman, R. Cox, H. Brenner, Slow viscous motion of a sphere parallel to a plane wall—II couette flow, Chem. Eng. Sci. 22 (1967) 653–660, http://dx.doi.org/10.1016/0009-2509(67)80048-4.

[22] R. Mei, An approximate expression for the shear lift force on a spherical particle at finite reynolds number, Int. J. Multiph. Flow 18 (1992) 145–147, http://dx.doi.org/10.1016/0301-9322(92)90012-6.

[23] D.S. Dandy, H.A. Dwyer, A sphere in shear flow at finite reynolds number: effect of shear on particle lift, drag, and heat transfer, J. Fluid Mech. 216 (1990) 381–410, http://dx.doi.org/10.1017/S0022112090000477.

[24] S.I. Rubinow, J.B. Keller, The transverse force on a spinning sphere moving in a viscous fluid, J. Fluid Mech. 11 (447) (1961) http://dx.doi.org/10.1017/S0022112061000640.

[25] C.T. Crowe, J.D. Schwarzkopf, M. Sommerfeld, Y. Tsuji, Multiphase flows with droplets and particles, 2011, http://dx.doi.org/10.1201/b11103.

[26] B. Oesterle, A. Petitjean, Simulation of particle-to-particle interactions in gas solid flows, Int. J. Multiph. Flow 19 (1993) 199–211, http://dx.doi.org/10.1016/0301-9322(93)90033-Q.

[27] H. Ounis, G. Ahmadi, J.B. McLaughlin, Brownian diffusion of submicrometer particles in the viscous sublayer, J. Colloid Interface Sci. 143 (1991) 266–277, http://dx.doi.org/10.1016/0021-9797(91)90458-K.

[28] M. Sommerfeld, Some open questions and inconsistencies of Lagrangian particle dispersion models, in: Proc. of 9th Symp. on Turbulent Shear Flows, Vol. 15, 1993.

[29] F. Lizal, M. Belka, J. Adam, J. Jedelsky, M. Jicha, A method for in vitro regional aerosol deposition measurement in a model of the human tracheobronchial tree by the positron emission tomography, Proc. Inst. Mech. Eng., H: J. Eng. Med. 229 (2015) 750–757, http://dx.doi.org/10.1177/0954411915600005.

[30] B.D. Alexander, T.P. Winkler, S. Shi, E.S.D. Ashley, Nebulizer delivery of micafungin aerosols, Pharmacother.: The J. Hum. Pharmacol. Drug Ther. 31 (2011) URL: https://api.semanticscholar.org/CorpusID:25364096.